British Antarctic Survey's Aerogeophysical Data: Releasing 25 Years of Airborne Gravity, Magnetic, and Radar Datasets over Antarctica

Alice C. Frémand[1*], Julien A. Bodart[1, 2*], Tom A. Jordan[1], Fausto Ferraccioli[1, 3], Carl Robinson[1], Hugh F.J. Corr[1], Helen J. Peat[1], Robert G. Bingham[2], and David G. Vaughan[1]

[1] British Antarctic Survey, Cambridge, UK.
[2] School of GeoSciences, University of Edinburgh, Edinburgh, UK.
[3] Istituto Nazionale di Oceanografia e di Geofisica Sperimentale, Trieste, Italy

* These authors contributed equally to this work.

Corresponding authors: Alice C. Fremand (almand@bas.ac.uk) and Julien A. Bodart (julien.bodart@ed.ac.uk)

Key Points

- We present the release of 64 aerogeophysical datasets (including gravity, magnetic, bed-pick, and radar data) obtained from 24 surveys flown by the British Antarctic Survey over West Antarctica, East Antarctica, and the Antarctic Peninsula between 1994 and 2020.

- The published datasets have been standardised according to the FAIR (Findable, Accessible, Interoperable and Re-Usable) data principles and integrated into a user-friendly data interface, the Polar Airborne Geophysics Data Portal, to further enhance the interactivity of the datasets.

- We discuss how the data were acquired and processed and, using a layer-continuity method, show potential avenues for future studies attempting to extract further information from the englacial architecture of the ice using the radar data.

Abstract

Over the past 50 years, the British Antarctic Survey (BAS) has been one of the major acquirers of aerogeophysical data over Antarctica, providing scientists with gravity, magnetic and radar datasets that have been central to many studies of the past, present, and future evolution of the Antarctic Ice Sheet. Until recently, many of these datasets were unpublished in full, restricting further usage of the data for different applications such as gravity inversions, bed-reflectivity analysis, and englacial-layer tracking. Starting in 2020, scientists and data managers at the British Antarctic Survey have worked on standardising and releasing large swaths of aerogeophysical data acquired during the period 1994-2020, including a total of 64 datasets from 24 different surveys, amounting to ~450,000 line-km (or 5.3 million km^2) of data across West Antarctica, East Antarctica, and the Antarctic Peninsula. Amongst these are the extensive surveys over the fast-changing Pine Island (BBAS 2004-05) and Thwaites (ITGC 2018-20) glacier catchments, and the first ever surveys of the Wilkes Subglacial Basin (WISE-ISODYN 2005-06) and Gamburtsev Subglacial Mountains (AGAP 2007-09). Considerable effort has been made to standardise these datasets to comply with the FAIR (Findable, Accessible, Interoperable and Re-Usable) data principles, as well as to create the Polar Airborne Geophysics Data Portal (https://www.bas.ac.uk/project/nagdp/), which serves as a user-friendly interface to interact with and download the newly published data. This paper reviews how these datasets were acquired and processed, presents the methods used to standardise them, and introduces the new data-portal infrastructure and interactive tutorials that were created to improve the accessibility of the data. Lastly, we exemplify future potential uses of the datasets by extracting information on the continuity of englacial layering from the fully processed radar data. We believe this newly released data will be a valuable asset to future geophysical and glaciological studies over Antarctica and will extend significantly the life cycle of the data. All datasets included in this data release are now fully accessible at: https://data.bas.ac.uk.

Key Words: Aerogeophysics, Gravity, Magnetics, Radar, Antarctica, Airborne, Ice Thickness, Data, FAIR

1. Introduction

As one of the fastest changing environments on Earth, Antarctica has been at the epicentre of scientific research since the early 1960s. Understanding the past, present, and future of the Antarctic Ice Sheet is of special interest, particularly in the context of rapid climatic changes already affecting large parts of the Antarctic Peninsula and threatening the stability of the West Antarctic Ice Sheet (IPCC, 2021). One way to quantify how the ice sheet will respond to these changes is to conduct surveys of the ice and bedrock underneath using geophysical techniques such as gravity, magnetic, and radar. By studying the bed beneath an ice sheet, we can better estimate where a retreating ice stream is more likely to stabilise or de-stabilise further (Holt et al., 2006; Morlighem et al., 2020; Ross et al., 2012; Tinto and Bell, 2011; Vaughan et al., 2006) and how topography or subglacial water-routing systems can affect the flow-regime of ice streams (Ashmore and Bingham, 2014; Bell et al., 2011; Schroeder et al., 2013; Siegert et al., 2014; Wright et al., 2012; Young et al., 2016). By studying the subglacial geology underlying the ice, we can better understand magmatic, tectonic and sedimentary influences on ice flow over timescales of hundreds, thousands or even millions of years (Bamber et al., 2006; Bell et al., 1998; 2006; Bingham et al., 2012; Blankenship et al., 2001; Jordan et al., 2010; Studinger et al., 2001), and quantify the influence of geothermal heat flux on ice dynamics (Jordan et al., 2018; Schroeder et al., 2014). Finally, the use of gravity techniques enables us to better understand the bathymetry beneath fast-changing ice shelves and ice-stream fronts and quantify areas of high sensitivity (Greenbaum et al., 2015; Jordan et al., 2020; Millan et al., 2017; Tinto et al., 2019).

Since the mid-1960s, the British Antarctic Survey (BAS) has been involved in acquiring aerogeophysical data with a particular focus on radar-data acquisition using a 35- and 60-MHz radio-echo sounder developed at the Scott Polar Research Institute (Robin et al., 1970), and, in collaboration with the Technical University of Denmark, using slightly improved versions of the same analogue radar system until the early 1990s (Robin et al., 1977). The subsequent development of an in-house digital radar system at BAS in 1993-94 (Corr and Popple, 1994), and accompanying gravity and magnetic instruments, allowed for the first surveys over West Antarctica's Evans Ice Stream to be conducted in 1994-95, marking the start of modern aerogeophysical surveying of the Antarctic by BAS. Further improvements in survey techniques and instruments have allowed BAS to develop its aerogeophysical capabilities further and become one of the leaders in aerogeophyics over the Antarctic.

Since the mid-1990s, aerogeophysical datasets acquired by BAS have been playing a vital role in understanding past and current ice-dynamical and lithospheric processes over the Antarctic Ice Sheet. In total, BAS flew 24 survey campaigns between 1994 and 2020, representing a total of ~450,000 line-km of aerogeophysical data over the Antarctic Peninsula and the West and East Antarctic Ice Sheets (hereafter abbreviated to WAIS and EAIS respectively) (Fig. 1, Table 1). The total cumulative survey coverage since 1994 is 5.3 million km^2, equivalent to > 30 % of the total area of the Antarctic Ice Sheet (14.2 million km^2). Many of these surveys were acquired as part of large international collaborative projects such as the International Polar Year AGAP project, the European Space Agency (ESA) PolarGAP project, and the US-UK International Thwaites Glacier Collaboration (ITGC), amongst others, while much of the data have been central to the output of large international science groups, such as the SCAR-funded (Scientific Committee on Antarctic Research) BEDMAP (I/II/III), ADMAP (I/II), AntArchitecture, and IBCSO projects (Arndt et al., 2013; Fretwell et al., 2013; Golynsky et al., 2018; Lythe et al., 2001).

104
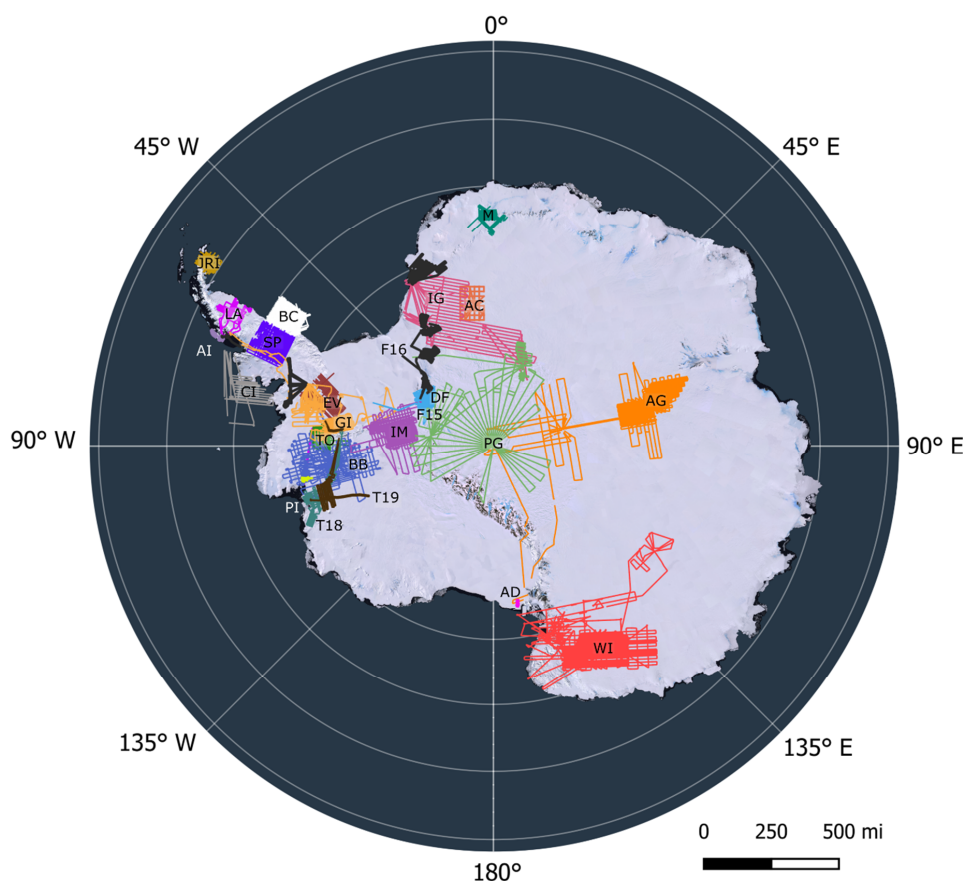
Figure 1. Map showing all the published datasets included in this data release. The colours are the same as those used on the data portal interface. Abbreviations are as follows: EV: EVANS (1994-95); BC: Black Coast (1996-97); CI: Charcot Island (1996-97); JRI: James Ross Island (1997-98); LA: Larsen Ice Shelf (1997-98); DF: DUFEK (1998-99); AC: AFI Coats Land (2001-02); M: MAMOG (2001-02); TO: TORUS (2001-02); SP: SPARC (2002-03); BB: BBAS (2004-05); WI: WISE-ISODYN (2005-06); GI: GRADES-IMAGE (2006-07); AG: AGAP (2007-09); AD: Andrill HRAM (2008-09); AI: Adelaide Island (2010-11); IM: IMAFI (2010-11); PI: Pine Island Glacier Ice Shelf (2010-11); IG: ICEGRAV (2012-13); F15: FISS 2015 (2015-16); PG: PolarGAP (2015-16); F16: FISS-EC-Halley 2016 (2015-16); T18: ITGC Thwaites (2018-19); T19: ITGC Thwaites (2019-20). The background image is from the Landsat Image Mosaic of Antarctica (LIMA; Bindschadler et al., 2008).

Despite the importance of these surveys to understanding the Antarctic cryosphere and tectonics, until now the underlying data have been relatively inaccessible to the wider geophysical and glaciological communities due to the scale of the data-management task required. As a result, this lack of accessibility has hampered the ability of the wider research community to extract further valuable information from these datasets. In 2020, a collaborative project between the UK Polar Data Centre (PDC, https://www.bas.ac.uk/data/uk-pdc/) and the BAS Airborne Geophysics science team was set up to improve the FAIR-ness (Findability, Accessibility, Interoperability and Re-Usability; Wilkinson et al., 2016) of these data. The main objectives of this collaboration were to comply with national and international policies on data sharing and accessibility, foster new collaborations, and allow the further re-use of these data beyond the lifespan of the science projects.

125   This paper presents the result of this successful collaboration between data managers and
126   scientists to standardise and release most of BAS' aerogeophysical data acquired to date using modern
127   instruments from 1994 onwards. Data acquired prior to this, while particularly useful to long-term
128   monitoring of ice sheet conditions, are much more challenging and time-consuming to bring up to
129   modern standards (see Schroeder et al., 2019; Sect 5.3), and are thus not included in the data release
130   discussed here. Section 2 of this paper reviews the main scientific findings from each survey flown
131   between 1994 and 2020. Section 3 describes the various instruments and techniques used to acquire
132   and process the data. Section 4 outlines the format and data publishing strategy for our datasets
133   following the FAIR data principles, as well as the creation of a new data portal and interactive, open-
134   access tutorials. Finally, Section 5 discusses potential avenues for future data analyses, focusing
135   primarily on extracting further information from the radar data.

136

2.   Background

138   The following section reviews the main scientific findings related to the acquisition of
139   aerogeophysical data from BAS for the period 1994-2020 and is divided into two sections: findings
140   from surveys conducted pre-2004 using older aerogeophysical instruments, and surveys conducted
141   post-2004 using the PASIN- (Polarimetric Airborne Survey INstrument) 1 (2004-2015) and PASIN-2
142   (2015-2020) radar systems and more modern data acquisition methods. Figures 2-3 demonstrate that
143   the surveys discussed in these sections have been used progressively to build up wide-ranging datasets
144   of gravity and magnetic anomalies, bed elevation and ice thickness, and 2-D radar profiles that we
145   release with this paper.

2.1. Aerogeophysical Surveys for the Period 1994-2004

147   The first surveys conducted by BAS since the mid-1990s involved extensive gravity and
148   magnetic surveying of the western and eastern Antarctic Peninsula and Weddell Sea Embayment.
149   Surveys over Evans Ice Stream (1994-95), Black Coast (1996-97), Charcot Island (1996-97), and
150   James Ross Island (1997-98) (Fig. 1, Table 1) provided new insights into the history of crustal
151   boundaries between the eastern Antarctic Peninsula and the Filchner Block (Ferris et al., 2002),
152   evidence of crustal thinning below Evans Ice Stream (Jones et al., 2002), and new understanding of
153   the magmatic and tectonic processes around the Mount Haddington stratovolcano on James Ross
154   Island (Jordan et al., 2009). A further study covering the Larsen Ice Shelf (Antarctic Peninsula) was
155   conducted conjointly by BAS and Instituto Antártico Argentino in 1997-98. The radar data acquired
156   during this survey was used in ocean (Holland et al., 2009) and firn-density (Holland et al., 2011)
157   models to improve our understanding of ice-ocean interactions and ice-surface elevation change on
158   the ice shelf. In 1998-99, extensive aeromagnetic surveying of the Dufek Massif (West Antarctica)
159   revealed the presence of a Jurassic dyke swarm that likely acted as a magma transport and feeder
160   system to the Ferrar Large Igneous Province (Ferris et al., 2003). In 2001-02, an additional survey
161   was flown over the Rutford Ice Stream basin as part of the TORUS (Targeting ice-stream Onset
162   Regions and Under-ice Systems) initiative, acquiring gravity, magnetic and radar data in a high-
163   resolution grid with ~10-km across-track spacing between radar lines. The SPARC (Superterranes of
164   the Pacific Margin Arc) campaign of 2002-03 over Northern Palmer Land (Antarctic Peninsula) used
165   gravity and magnetic instruments to reveal subglacial imprints of crustal growth linked with the
166   Gondwana margin (Ferraccioli et al., 2006).

167   Over East Antarctica, two surveys conducted in 2001-02 acquired detailed gravity, magnetic
168   and radar measurements over Slessor Glacier (AFI; Antarctic Funding Initiative Coats Land survey)
169   and Jutulstraumen Ice Stream (MAMOG; Magmatism as a Monitor of Gondwana break-up). The AFI
170   Coats Land survey provided the first accurate measurements of ice thickness and bed elevation in the
171   area (Rippin et al., 2003a) (Fig. 2), and led to the discovery of a ~3-km thick sedimentary basin

172 associated with a weak till layer at the bed which enhances basal motion and affects the flow regime
173 of this part of the EAIS (Bamber et al., 2006; Rippin et al., 2003a; Shepherd et al., 2006). The
174 MAMOG survey revealed the presence of a subglacial Jurassic continental rift in the area of western
175 Dronning Maud Land, providing early evidence for the initial Gondwana break up (Ferraccioli et al.,
176 2005a; 2005b).

177 **2.2. Aerogeophysical Surveys for the Period 2004-2020**

178 Building from the surveys prior to 2004 which were relatively small in coverage, BAS began
179 surveying larger areas from the mid-2000s onwards (Table 1), primarily due to enhanced international
180 collaborations and improvements in data acquisition and instruments which led to data being acquired
181 both at higher resolution and over larger spatial scales (Fig. 4-5). The acquisition strategy was to
182 collect data from multiple geophysical sensors mounted on BAS' Twin Otter aircraft across every
183 survey, giving a holistic view of vast and previously unsurveyed regions. The core sensor suite
184 included gravity and magnetic instruments used to understand the sedimentary nature of the basins
185 and their techonomic structure, alongside the radar system used to map ice thickness and bed
186 elevation. The development of a new radar system, the Polarimetric Airborne System Instrument
187 (PASIN) (PASIN-1, 2004-2015) (see Sect. 3.1.3), and an improved version of the same system
188 (PASIN-2, 2015-16 onwards), allowed for the efficient collection of high-quality digital radar data for
189 BAS-led campaigns in the Antarctic.

190 We describe the findings from these surveys in more details below, starting with the
191 campaigns conducted between 2004-2015 (Sect. 2.2.1), and then followed by the campaigns
192 conducted between 2015-2020 (Sect. 2.2.2).

193 **2.2.1 2004-2015**

194 The first mission to utilise the PASIN-1 radar system was the 2004-05 BBAS survey of Pine
195 Island Glacier (Vaugan et al., 2006). This survey provided two key findings: a) the discovery of a
196 deep subglacial trough, 500 m at its deepest point and 250 km long, through which Pine Island Glacier
197 flows; and b) the existence of well-constrained valley walls which would likely provide a buffer
198 against a potential catastrophic collapse of the WAIS via Pine Island Glacier (Vaughan et al., 2006).
199 Further studies utilising this dataset focused primarily on bed characteristics and the subglacial
200 hydrology of the catchment (Chu et al., 2021; Napoleoni et al., 2020; Rippin et al., 2011), as well as
201 tracking englacial layers and quantifying past-accumulation rates (Bodart et al., 2021; Corr and
202 Vaughan, 2008; Karlsson et al., 2009; 2014). The survey was also conducted simultaneously with
203 another covering the Thwaites Glacier catchment led by the University of Texas Institute for
204 Geophysics and the National Science Foundation of the United States (Holt et al., 2006), enabling a
205 comparison of the surveying capabilities where the surveys overlapped (e.g. Chu et al., 2021).

206 **Table 1. Information on the period, region, sub-region, type of data acquired, total line-coverage**
207 **(km), total coverage area (km²), and key reference for each survey included in this data release.** For
208 "Data", the abbreviations are as follows: Gravity (G), Magnetic (M), Radar (R). For "Regions", abbreviations
209 are as follows: APIS (Antarctic Peninsula Ice Sheet), EAIS (East Antarctic Ice Sheet), WAIS (West Antarctic
210 Ice Sheet). "DML" stands for Dronning Maud Land and "PIG" for Pine Island Glacier. The total area in km² is
211 calculated as a cumulative total area of the spatial footprint of the survey's minimum and maximum extent.

Survey	Year	Region	Sub-Region	Data	Total line coverage (km)	Total coverage area (km²)	Reference
EVANS	1994-95	WAIS	Evans Ice Stream	G, M, R	11500	1.06 x10⁵	Jones et al. (2002)
Black Coast	1996-97	APIS	Black Coast/ Weddell Sea	M	10000	8.96 x10⁴	Ferris et al. (2002)
CHARCOT	1996-97	APIS	Charcot Island	M	7500	1.67 x10⁵	Johnson et al. (1999)

Name	Years	Region	Location	Instruments	Line km	Area (km²)	Reference
James Ross Island	1997-98	APIS	James Ross Island	G, M, R	10000	3.32×10^4	Jordan et al. (2009)
LARSEN	1997-98	APIS	Larsen Ice Shelf	M, R	5800	5.96×10^4	Holland et al. (2009)
DUFEK	1998-99	WAIS	Dufek Massif	G, M, R	8300	4.66×10^4	Ferris et al. (2003)
AFI Coats Land	2001-02	EAIS	Slessor Glacier	G, M, R	5000	6.53×10^4	Rippin et al. (2003a)
MAMOG	2001-02	EAIS	Jutulstraumen Ice Stream / DML	G, M, R	15500	5.79×10^4	Ferraccioli et al. (2005a)
TORUS	2001-02	WAIS	Rutford Ice Stream	G, M, R	8600	1.12×10^5	-
SPARC	2002-03	APIS	Northern Palmer Land	G, M	20000	1.07×10^5	Ferraccioli et al. (2006)
BBAS	2004-05	WAIS	Pine Island Glacier	G, M, R	35000	4.09×10^5	Vaughan et al. (2006)
WISE-ISODYN	2005-06	EAIS	Wilkes Land	G, M, R	61000	7.91×10^5	Jordan et al. (2013)
GRADES-IMAGE	2006-07	WAIS/ APIS	Evans & Rutford ice streams	M, R	27500	3.06×10^5	Ashmore et al. (2014)
AGAP	2007-09	EAIS	Gamburtsev / Dome A	G, M, R	73000	6.22×10^5	Ferraccioli et al. (2011)
ANDRILL HRAM	2008-09	WAIS	Ross Ice Shelf & Coulman High	M, R	1200	1.48×10^3	-
Adelaide Island	2010-11	APIS	Adelaide Island	M, R	5500	3.76×10^3	Jordan et al. (2014)
IMAFI	2010-11	WAIS	Institute & Möller ice streams	G, M, R	25000	1.96×10^5	Ross et al. (2012)
PIG Ice Shelf	2010-11	WAIS	Pine Island Shelf	M, R	1500	1.80×10^3	Vaughan et al. (2012)
ICEGRAV	2012-13	EAIS	Recovery & Slessor glaciers, Bailey Ice Stream	G, M, R	29000	4.75×10^5	Diez et al. (2018)
FISS 2015	2015-16	WAIS	Foundation Ice Stream / Bungenstock Ice Rise	M, R	7000	1.43×10^4	-
PolarGAP	2015-16	EAIS	South Pole	G, M, R	38000	8.71×10^5	Jordan et al. (2018)
FISS 2016	2016-17	WAIS	Filchner Ice Shelf / English Coast / Recovery & Support Force glaciers / Halley station	G, M, R	26000	5.99×10^5	Hofstede et al. (2021)
ITGC 2018	2018-20	WAIS	Thwaites Glacier	G, M, R	9872	6.43×10^4	Jordan et al. (2020)
ITGC 2019	2019-20	WAIS	Thwaites Glacier / WAIS Divide / Rutford Ice Stream	G, M, R	4432	4.85×10^4	-

212

213   Following on from the BBAS survey, the suite of geophysical instruments on board the BAS
214 Twin Otter aircraft were used to survey Wilkes Subglacial Basin, Dome C, and the Transantarctic
215 Mountains as part of the 2005-06 WISE-ISODYN survey between BAS and the Italian Programma

216   Nazionale di Ricerche in Antartide (Bozzo and Ferraccioli, 2007; Corr et al., 2007; Ferraccioli et al.,
217   2007; Jordan et al., 2007). This project revealed, for the first time, the crustal architecture of the
218   Wilkes Subglacial Basin (Ferraccioli et al., 2009; Jordan et al., 2013) and the distribution of a well-
219   preserved subglacial sedimentary basin underlying the Wilkes catchment (Frederick et al., 2016). The
220   following year, the 2006-07 GRADES-IMAGE (Glacial Retreat in Antarctica and Deglaciation of the
221   Earth System - Inverse Modelling of Antarctica and Global Eustasy) survey, comprising surveys over
222   the transitional area between the Antarctic Peninsula and the WAIS, provided detailed information on
223   subglacial properties of Evans Ice Stream (Ashmore et al., 2014), ice-thickness measurements along
224   the grounding line were used as key calibration for the Landsat-derived "ASAID" grounding-line
225   product (Bindschadler et al., 2011), and englacial layers through Bungenstock Ice Rise were used to
226   assess ice-divide stability and the wider ice-flow history and stability of the WAIS's Weddell Sea
227   sector during the Holocene (Siegert et al., 2013).

228   Over two austral field seasons from 2007 to 2009, the AGAP (Antarctica's Gamburtsev
229   Province Project) survey, coordinated as part of the fourth International Polar Year between the UK,
230   USA, Germany, Japan, Australia and China, comprised a comprehensive survey of the interior of the
231   EAIS, yielding important aerogeophysical data used to interrogate the origin and geophysical
232   characteristics of the Gamburtsev Subglacial Mountains. Significant scientific discoveries generated
233   by the AGAP survey included observations of widespread freeze-on at the bottom of the ice which
234   leads to thickening of the EAIS from the base (Bell et al., 2011), a thick crustal root formed during the
235   Proterozoic aeon (1 Gyr ago) surrounded by a more recent ~2,500-km-long rift system (Ferraccioli et
236   al., 2011), and the existence of ancient pre-glacial fluvial networks at the present ice bed which
237   confirmed the presence of the Gamburtsevs prior to the start of glaciation at the Eocene–Oligocene
238   climate boundary (ca. 34 Ma) (Creyts et al., 2014; Rose et al., 2013).

239   Between 2008 and 2011, three surveys utilised the magnetic and radar instruments on board
240   the BAS Twin Otter to conduct high-spatial resolution surveying of Coulman High on Ross Ice Shelf
241   as part of the ANDRILL HRAM (Antarctic Drilling - High Resolution Aeromagnetic) project,
242   Adelaide Island (Antarctic Peninsula), and Pine Island Glacier Ice Shelf (West Antarctica). The 2010-
243   11 Adelaide Island survey provided high-resolution aeromagnetic data to underpin a better
244   understanding of the complex magmatic structure of the Antarctic Peninsula Cenozoic arc/forearc
245   boundary (Jordan et al., 2014). The Pine Island Glacier Ice Shelf survey of the same year revealed a
246   network of sinuous subglacial channels, 500- to 3000-m wide and up to 200-m high, in the ice-shelf
247   base, which, combined with surface and basal crevasses formed as a result of the basal melting, could
248   lead to structural weakening of the shelf in the future (Vaughan et al., 2012).

249
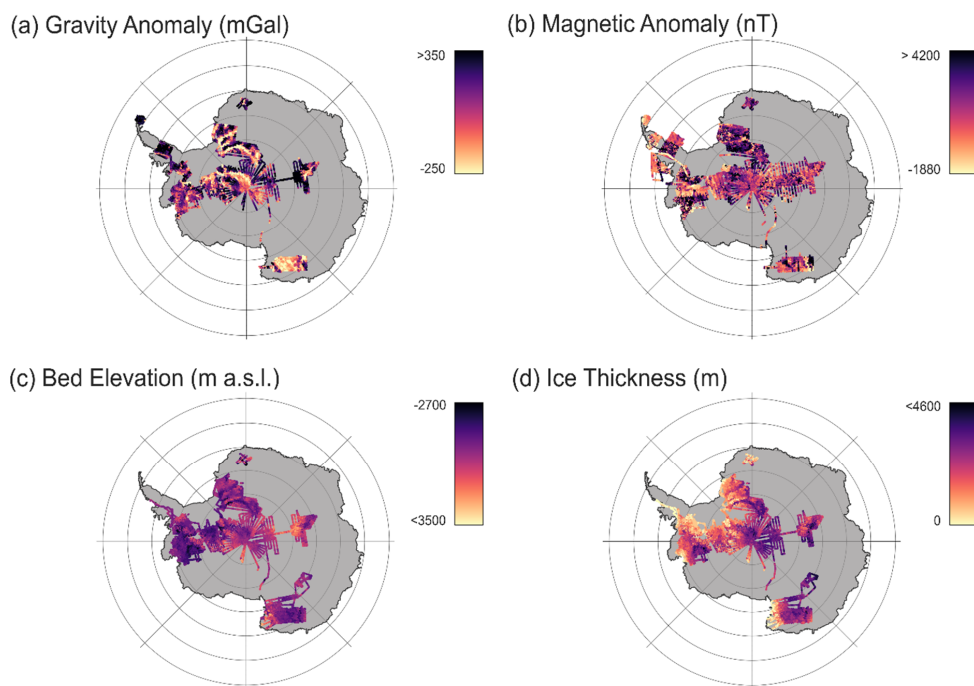
250
251   **Figure 2. Maps of gravity, magnetic, and radar (bed elevation and ice thickness) point**
252 **measurements for all surveys published as part of this data release.** (a) Gravity anomaly points (in milligal,
253 or mGal), (b) Magnetic anomaly points (in nanotesla, or nT), (c) Bed elevation points from radar data (in metres
254 above sea level, or m a.s.l.), (d) Ice thickness points from radar data (metres). In total, this data release contains
255 3.62 million gravity, 7.41 million magnetics, and 14.5 million ice-thickness and bed-elevation data points. Note
256 that no correction such as downward continuation has been applied to compile the gravity data shown in (a).

257   The early 2010s saw the deployment of the PASIN system used as part of two large
258 collaborative projects, namely the 2010-11 Institute-Möller Antarctic Funding Initiative (IMAFI)
259 survey over Institute and Möller ice streams of West Antarctica, and the 2012-13 ICEGRAV survey
260 over the Recovery and Slessor region of East Antarctica.

261   The 2010-11 IMAFI project was designed to assess the ability of the subglacial sedimentary
262 structure to control the flow of two large ice streams draining the WAIS into the Weddell Sea
263 Embayment, and the potential stability of this sector of West Antarctica (Ross et al., 2012). Radar
264 data revealed the presence of a reverse-bed slope with a 400-m decline over a 40-km distance away
265 from the grounding line and that this region was relatively close to flotation, indicating the potential
266 instability of this sector in the light of future grounding-line migration upstream of its current position
267 (Ross et al., 2012). Additional analysis using gravity and magnetic data revealed the extent of the
268 Weddell Sea Rift, adding further evidence for the early-stages of Gondwana break-up and Jurassic
269 extension in the region (Jordan et al., 2013). Further analysis of the radar data acquired during the
270 IMAFI survey led to a new digital elevation model of the bed underlying the ice streams of the
271 Weddell Sea Embayment at 1-km resolution, revealing deep subglacial troughs between the ice-sheet
272 interior and the grounding line and well-preserved landforms associated with alpine glaciation (Jeofry
273 et al., 2018; Ross et al., 2014), as well as evidence for a temperate former WAIS via the discovery of
274 extensive subglacial meltwater channels (Rose et al., 2014). The data have also been used to assess

275 bed roughness (Rippin et al., 2014) and englacial properties across the catchment in order to elucidate
276 past ice-flow dynamics (Ashmore et al., 2020; Bingham et al., 2015; Winter et al., 2015).

277   The 2012-13 ICEGRAV survey, the product of an international collaboration between BAS
278 and the Technical University of Denmark, National Science Foundation, Norwegian Polar Institute,
279 and the Instituto Antártico Argentino, carried out aerogeophysical surveys over the poorly explored
280 Recovery Glacier catchment and Recovery Subglacial Lakes (Forsberg et al., 2018), revealing a deep
281 800-km trough underlying Recovery Glacier, with evidence for subglacial water controlling the fast
282 flow in the upstream portion of the ice stream (Diez et al., 2018).

283   **2.2.2 2015-2020**

284   The 2015-16 PolarGAP survey, the first to deploy a further upgraded radar system, PASIN-2
285 (see Sect. 3.1.3), was a major international collaboration funded by the European Space Agency
286 (ESA) and led by BAS, Technical University of Denmark, Norwegian Polar Institute and the National
287 Science Foundation designed primarily to fill a gap in global gravity surveying that the European
288 Space Agency GOCE (Gravity field and steady-state Ocean Circulation Explorer) satellite network
289 was unable to cover. Alongside the large swath of gravity surveying, opportunistic magnetic and radar
290 data were also acquired over the South Pole and parts of Support Force, Foundation, and Recovery ice
291 streams. Additional funding from the Norwegian Polar Institute also allowed for a number of
292 dedicated flights over the subglacial Recovery Lakes. The acquired data have led to major scientific
293 findings, such as the presence of anomalously high geothermal heat flux near the South Pole (Jordan
294 et al., 2018) and the delineation of two active subglacial lakes (Recovery Lakes A and B) totalling
295 ~4,320 km^2 in size and composed of saturated till, with evidence of bed lubrication and enhanced flow
296 downstream of their location as a result of water drainage (Diez et al., 2019). Additional evidence
297 showed that the Pensacola-Pole Basin is characterised by a topographic depression of ~0.5 km below
298 sea level and contains a thick sedimentary layer of 2-3 km in the southern part of the catchment
299 (Paxman et al., 2019). The radar data from the PolarGAP survey have also revealed large troughs at
300 the bottleneck between East and West Antarctica, suggesting that drawdown of the EAIS via the
301 WAIS is unlikely (Winter et al., 2018).

302   In the austral summers of 2015-16 and 2016-17, two surveys were flown as part of the
303 Filchner Ice Shelf System (FISS) project with support from the Alfred-Wenger Institute, Germany,
304 with the aim to investigate the potential contribution of the Filchner Ice Shelf system to sea-level rise.
305 The 2015-16 survey acquired ~7,000 line-km of aerogeophysical data over Foundation Ice Stream and
306 Bungenstock Ice Rise. In 2016-17, ~26,000 line-km of aerogeophysical data were acquired over
307 Filchner and Brunt ice shelves (West Antarctica), as well as over outlet glaciers of English Coast
308 (western Palmer Land, Antarctic Peninsula). Early findings from the 2016-17 aerogeophysical survey
309 revealed subglacial drainage channels beneath Support Force Glacier (Hofstede et al., 2021), provided
310 evidence for a large ~80 x 30 x 6 km mafic intrusion likely resulting from mantle melting during
311 Gondwana break-up (Jordan and Becker, 2018), and helped to delineate the subglacial bathymetry
312 beneath Brunt Ice Shelf (Hodgson et al., 2019).

313   During the 2018-19 and 2019-20 seasons, BAS was involved in aerogeophysical surveying of
314 Thwaites Glacier as part of the UK-US International Thwaites Glacier Collaboration (ITGC)
315 initiative. The 2018-19 survey acquired ~9,900 km of aerogeophysical data over lower Thwaites
316 Glacier and Thwaites Glacier Ice Shelf, and the 2019-20 survey acquired ~4500 line-km over lower
317 Thwaites Glacier, the WAIS Divide ice-core site, and Rutford Ice Stream. These surveys contributed
318 to a new bathymetric map of Thwaites, Crosson and Dotson ice shelves from gravity measurements,
319 revealing a deep (>800 m) marine channel extending beneath the ice shelf adjacent to the front of
320 Thwaites Glacier (Jordan et al., 2020). These datasets have also contributed to a new bathymetry
321 model of George VI Sound (Constantino et al., 2020) and Thwaites Glacier (Hogan et al., 2020).

322
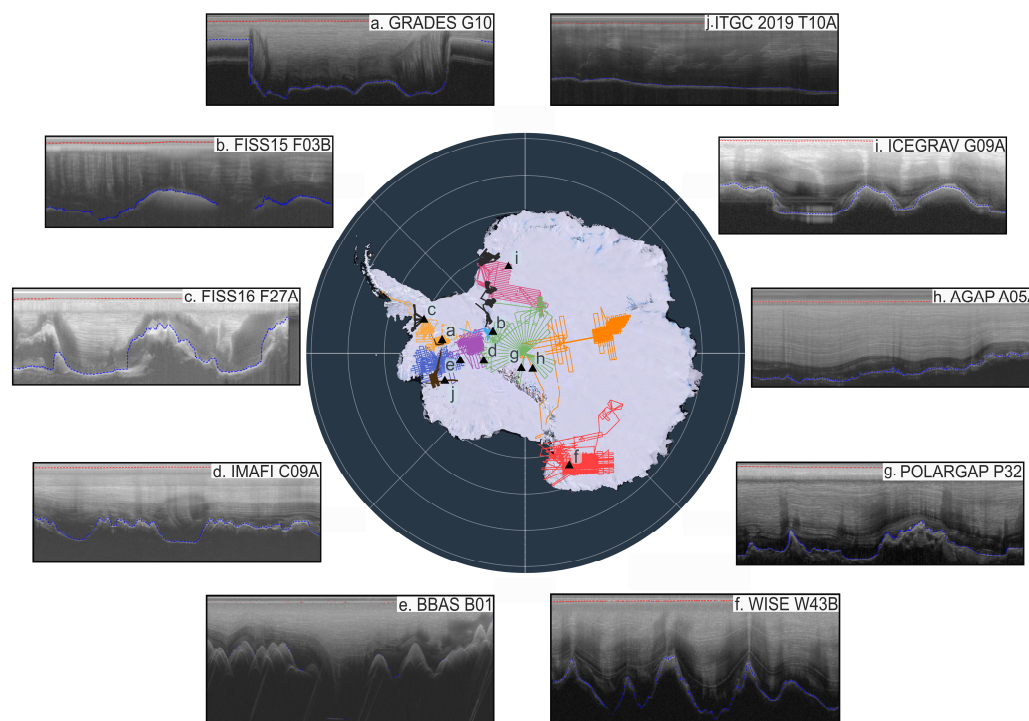
Figure 3. Sample radargrams from the ten 2-D radar datasets released with this paper. The colours for each survey on the map are the same as in Fig. 1 and the data portal. The location of each radargram (a-j) is marked on the map by black triangles. The red and blue dashed lines on the radargrams are the surface and bed picks respectively. A description of each radargram is provided as follows: (a) Flightline G10 (GRADES-IMAGE) showing well-defined subglacial valleys through which Evans Ice Stream flows (ice flow is approximately out of page), with stable layering at the onset and in the middle of the topographic low; (b) Flightline F03B (FISS 2015) showing undulating bed topography and disrupted layering at the onset of Foundation Ice Stream; (c) Flightline F27A (FISS 2016) showing variations in subglacial topography at the divide between the Antarctic Peninsula and West Antarctica, with potential evidence of basal freeze-on at the start of the segment; (d) Flightline C09A (IMAFI) showing evidence of preserved layering despite changes in local topography at the bottleneck between East and West Antarctica; (e) Flightline B01 (BBAS) over Ellsworth Subglacial Mountains showing a ~1.5 km trough in the ice sheet bed and one of the deepest points in the PIG basin with ~3km of ice underlying the surface; (f) Flightline W43B (WISE-ISODYN) showing internal layers draping over the highs and lows in the local Wilkes Subglacial Basin topography, with two particularly bright reflectors in the middle and bottom of the ice column; (g) Flightline P32 (PolarGAP) showing the onset of a topographic high near the Transantarctic Mountain Range with internal layering visible down to the ice-bed interface; (h) Flightline A05A (AGAP) showing stable internal layering characteristic of the interior of the EAIS; (i) Flightline G09A (ICEGRAV) showing evidence of a bright reflector likely associated with a previously unidentified subglacial lake in the region; and (j) Flightline T10A (ITGC 2019) showing a section of inland-sloping bed from a profile in the main trunk of Thwaites Glacier, >200 km from the current grounding line position (ice flow is right to left).

344

3. Data Acquisition and Processing

346   The typical acquisition and processing workflow for the aerogeophysical data is shown in
347 Figure 4. Generally, the aircraft is set up systematically to acquire gravity, magnetic, and radar data
348 together, except in situations where surveying objectives are not compatible with the acquisition of all

349   three datasets at once (i.e. flying at constant terrain clearance for the radar data affects the quality of
350   the gravity data which is better flown at constant altitude, and vice-versa); although novel gravity-
351   acquisition methods are increasingly making this issue redundant (see 3.1.1). As shown in Table 1, the
352   conventional gravity-magnetic-radar set-up was used in 19 out of 24 surveys, with the remaining 6
353   campaigns using either a magnetic-radar- or gravity-magnetic-only set-up. The data acquisition steps
354   for each type of data are described in Sect. 3.1, and the processing of the data is described in Sect. 3.2.
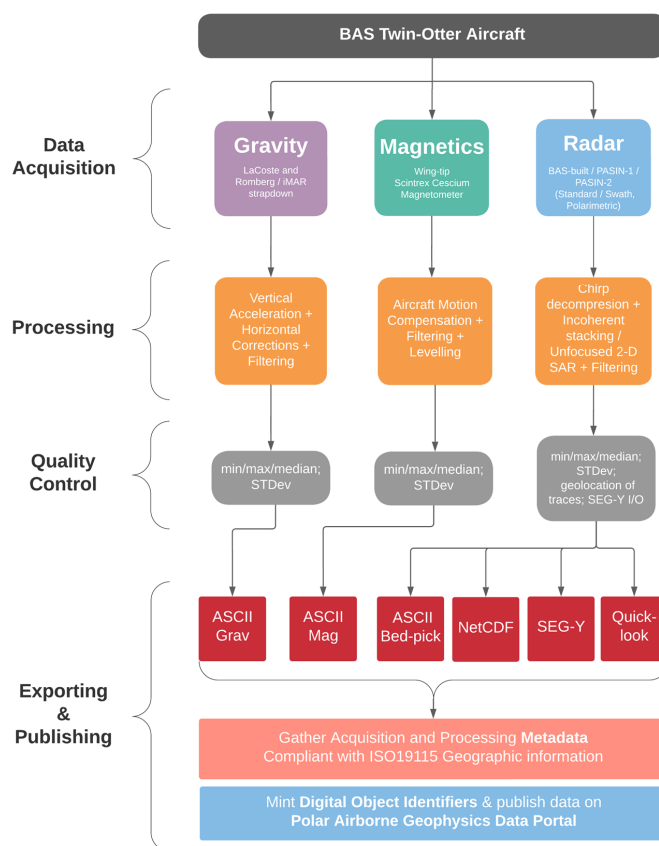
355

356   **Figure 4. Workflow describing the data acquisition, processing, and publishing for the BAS**
357   **aerogeophysical data included in this data release.** "STDev" stands for standard deviation, whilst "I/O" refers
358   to the output of the SEG-Y files and the import of the files into seismic-interpretation software for quality check.

359   ### 3.1. Data Acquisition and Instrumentation

360   All of BAS aerogeophysical data acquisition is conducted using Twin Otter aircraft due to
361   their remote capabilities, long fuel range (up to 1,000 km), and operability. The aircraft's twin turbo-
362   prop engines enable it to conduct rapid take-off and landing and operate in small and remote airfields
363   commonly covered in snow and icy terrains using mounted skis. All data acquisition since the early
364   1990s has been conducted using the BAS DeHavilland Twin Otter aircraft "VP-FBL" (Fig. 5). The
365   aircraft typically flies at a nominal speed of ~60 m/s, which results in an along-track distance between
366   each stacked radar trace of 0.2 m (prior to processing). The following sections describe the acquisition
367   of the data for the gravity (3.1.1), magnetic (3.1.2), radar (3.1.3), and GPS and lidar (3.1.4)
368   instruments on board the aircraft.

369
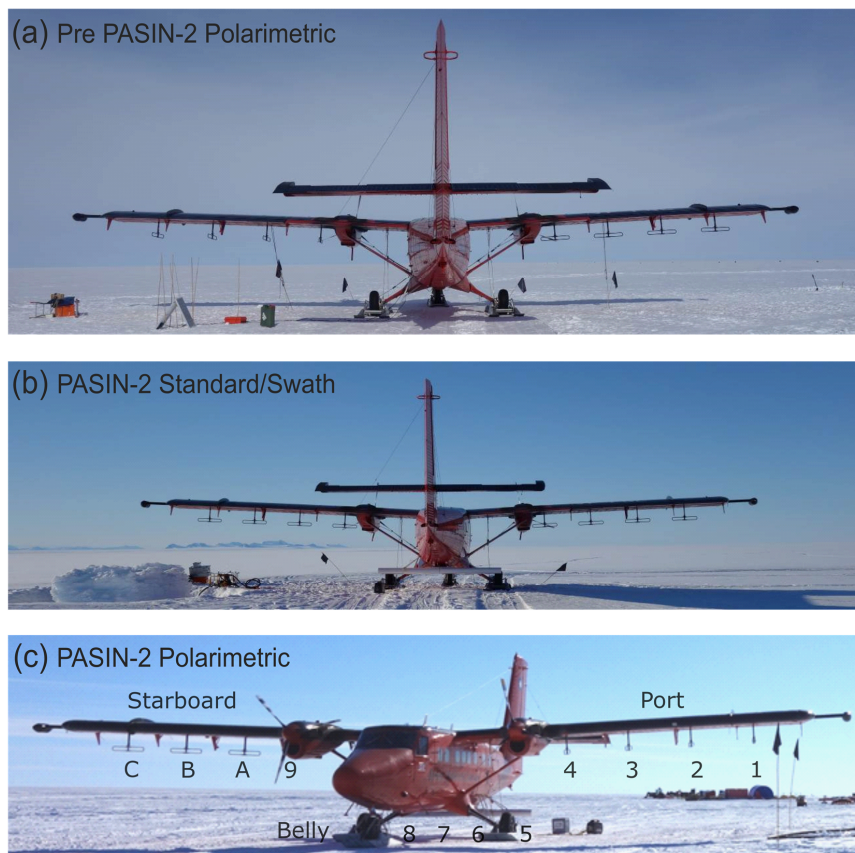
Figure 5. Photographs of the aerogeophysical set-up on the BAS Twin Otter aircraft "VP-FBL" for PASIN-2. The radar antennae and wing-tip magnetometers are visible on the wings. (a) The pre-PASIN-2 (used in 2015-16 PolarGAP only) configured to mimic the set-up of PASIN-1 data collection in polarimetric mode. The eight folded dipole transmitting and receiving antennae are fixed under the wings (two transmit and two receive antennae on each wing) with the port configured as V (vertical) and starboard as H (horizontal). (b) The PASIN-2 set-up in standard/swath mode. The twelve folded dipole transmitting and receiving antennae are fixed under the wings and inside the aircraft and are operated using an RF (Radio Frequency) switch, and an additional four receiving antennae are situated in the belly enclosure. When in standard swath mode, all antennae are configured in H orientation with the starboard and belly antennae also in H orientation. The PASIN-1 set-up in standard mode (not shown here) had a similar configuration as shown in (b) bar the belly antenna (i.e. only four transmit on port and four receive on starboard in H orientation) (c) The PASIN-2 set-up in polarimetric mode. The twelve folded dipole transmitting and receiving antennae are fixed under the wings and inside the aircraft and are operated using an RF switch, and an additional four receiving antennae are situated in the belly enclosure. When in polarimetric mode, the port antennae are configured in V orientation and the starboard and belly antennae in H orientation. The PASIN-1 set-up in polarimetric mode (not shown here as rarely flown) had the two pairs of outboard antennas rotated to V and the inboard in H configuration. Photo credit: Carl Robinson.

3.1.1 Gravity

388   Until 2012, BAS aerogravity measurements were acquired with a LaCoste and Romberg air-
389   sea gravimeter modified by Zero Length Spring Corporation (ZLS). The gravimeter was mounted in a
390   gyro-stabilised, shock-mounted platform at the centre of the aircraft to minimise the effect of
391   vibrations and rotational motions.

392   Starting with the 2015-16 PolarGAP survey, aerogravity data began to be aquired using a
393   novel strapdown method which, unlike traditional surveys using a stabilised gravity platform, allow
394   for the collection of gravity data during draped or turbulent flights (Jordan and Becker, 2018). For this
395   survey, both the LaCoste and Romberg and the strapdown systems were operated together with results
396   from the two systems merged to provide an optimum data product with the long-term low and
397   predictable drift of the LaCoste and Romberg system and dynamic stability of the strapdown system.
398   Subsequent surveys used a strapdown sensor alone, removing the need to prioritise the quality of the
399   gravity data over the radar data and allowing for flights at a constant terrain clearance for optimal
400   radar-data collection. The optimum resolution of the system is approximately 100 s along-track
401   (Jordan and Becker, 2018).

402   The first strapdown sensor deployed by BAS was the iMAR RQH-1003 provided by
403   Technical University (TU) Darmstadt, and consisting of three Honeywell QA2000 accelerometers
404   (mounted in mutually perpendicular directions) and three Honeywell GG1230 ring laser gyroscopes.
405   The subsequent 2018-19 and 2019-20 ITGC surveys over Thwaites Glacier used the iMAR iCORUS
406   strapdown airborne gravimeter systems from Lamont-Doherty Earth Observatory and BAS
407   respectively, which have approximately equivalent internal components to the TU Darmstadt system.

3.1.2 Magnetics

409   The Twin Otter is configured for fixed wing magnetometer operation. The aircraft
410   modifications include inboard-positioned wingtip fuel pumps, pod-boom hard points and a
411   demagnetised airframe to maximise magnetic-data collection. Scintrex CS3 Cesium sensors are used
412   due to their high sensitivity, high cycling rates, excellent gradient tolerance, fast response and low
413   susceptibility to the electromagnetic interference. The resolution of the magnetometers has greatly
414   increased over time, with the current systems having a measurement accuracy of 0.2 pT compared
415   with the older systems used between 1991-2003 (10 pT; Sintrex H8 Cesium) and 1973-1990 (500 pT;
416   Geometrics G-803 Potassium).

3.1.3 Radar

418   Prior to 2004, BAS deployed a custom-built, 8-array element radar system, referred here as
419   "BAS-built" (Corr and Popple, 1994). This was a coherent radar system operating at a centre
420   frequency of 150 MHz and using a transmit power of 1,200 W (Rippin et al., 2003a). The radar
421   system was equipped with eight folded dipole transmitting and receiving antennae fixed under the
422   wings (four transmitting on port wing, four receiving on starboard wing). Similar to the current
423   systems, the "BAS-built" system transmitted both a conventional narrow-sounding pulse mode of
424   0.25 μs and a deep-sounding 4μs, 10-MHz chirp (Table 2). As developments in digital acquisition
425   became commercially available, several technical upgrades were applied to the radar system. These
426   ranged from using a LeCroy scope to acquire logarithmic detected waveforms to complex coherent
427   acquisition, as well as the replacement of the LeCroy oscilloscope by a low sample-frequency 12-bit
428   dual ADC (analogue-to-digital converted) card in the later years of operation (see Fig. S1). During
429   this time, the dynamic range of the system was extended by the interleaved transmission of different
430   waveform, which were conventional short wavetrain pulses at the centre frequency.

431   After operating for ten successive field seasons, the "BAS-built" radar system was retired and
432   replaced by a more modern radar system, the Polarimetric Aiborne Survey INstrument (PASIN). In
433   contrast to the "BAS-built" system, PASIN was designed to sound ice much deeper (up to 5 km
434   compared with 3.3 km for the earlier system) thanks to improved digital electronics and added power

435 in the transmitting antennae (see Table 2). Additionally, the modern digitisation enabled by the use of
436 ADC cards rather than a digitising scope allowed phase and not just power to be recorded in greater
437 resolution on PASIN, which eventually allowed for the use of more advanced processing techniques
438 such as Synthetic-Aperture-Radar to be applied to the data (see Sect. 3.2.3).

439 The older PASIN-1 (2004-2015) and the newer PASIN-2 (2015-Present) systems are bi-static
440 radars operating at a 150-MHz centre frequency and configured as follows: (a) PASIN-1: 10-MHz
441 bandwidth system with eight folded dipole transmitting and receiving antennas fixed under the wings
442 (four transmitting on port wing, four receiving on starboard wing) operating in H (horizontal)
443 orientation when in standard mode and more rarely with the port (transmit) and starboard (receive)
444 antennae positioned in both H and V (vertical) orientation when in polarimetric mode (see similar
445 PASIN-2 set-up in Fig. 5a); and (b) PASIN-2: 13-MHz bandwidth system with twelve folded dipole
446 transmitting and receiving antennas fixed under the wings and inside the aircraft and operating using
447 an RF switch and an additional four receiving antennae in the belly enclosure (see Fig. 5b-c; Table 2).
448 When in standard/swath mode, the antennae are configure in H orientation (Fig. 5b) , whereas in
449 polarimetric mode the port antennae are configured in V orientation and the starboard and belly
450 antennae in H orientation (Fig. 5c). The main difference between the PASIN-1 and -2 systems is the
451 ability for across-track swath processing to be applied to the PASIN-2 data by allowing both transmit
452 and receive on the folded dipole antenna via the use of RF switches.

453 In further contrast with PASIN-1, the PASIN-2 radar has a very flexible configuration, with
454 the standard configuration being as a twelve channel swath radar (with eight transmit and twelve
455 receive). However, other configurations are also possible, including a polarimetric mode to give H
456 and V data where the port antennas are rotated 180 degrees (see Table S1). A final configuration is a
457 mixed antenna gain path for areas where ice is heavily disrupted where the starboard signal can be
458 attenuated by several decibels. Since 2016, the radar system has undergone minor modifications to
459 reduce noise and improve system operations, including low-pass filters in the RF switches, the use of
460 a 10-GHz waveform generator, and new 1 kW solid-state power amplifiers which have lowered
461 transmit system noise and increased transmitter and receiver isolation.

462 Data are received using sub-Nyquist digitisation and stacking and stored on removable solid-
463 state disks or tapes, and then copied to duplicate spinning disks for data archiving. On average, a 4.5-
464 hour flight will generate ~150-200 GB of data for PASIN-1 and up to 3 TB of data for PASIN-2. The
465 systems systematically acquire a shallow-sounding 0.1 μs pulse (PASIN-1) / 1 μs short-attenuated
466 chirp (PASIN-2), and a deep-sounding 4 μs, 10- (PASIN-1) /13- (PASIN-2) MHz linear chirp (Table
467 2). The shallow-sounding pulse/short-attenuated chirp product is best used to assess internal layering
468 in the upper ~1.5-2 km of the ice sheet, whereas the deeper-sounding chirp is best suited to assess
469 englacial layering and bed characteristics in deep-ice conditions (Fig. 6 a-b). The radar is capable of
470 sounding ice to depths of up to 5 km with a horizontal resolution of 10 cm (before processing) and a
471 depth resolution in the vertical direction of 8 m.

472 **Table 2. Radar Parameters for the three radar systems deployed by BAS between 1994 and the**
473 **Present.** Note that PASIN-1/2 have a number of programmable settings for flight-specific objectives (e.g. 1 to 8
474 waveforms programmable for PASIN-2), and the numbers provided here are for the most commonly used
475 settings. For PASIN-2, a standard set-up consists of 5 waveforms as follows: 4 μs H (0°), 4 μs V (0°), 4 μs H
476 (90°), 4 μs V (90°) ,1 μs H (Table S1). Abbreviations in the table are as follows: ADC = Analogue to Digital
477 Converter; FPGA = Field Programmable Gate Array; SF = Sample Frequency; SI = Sample Interval; PRF =
478 Pulse-Repetition Frequency; PRI = Pulse Repetition Interval. *BAS-built and PASIN-1 systems used RF
479 combiners on the receiver to produce a single RF input-to-sample, with PASIN-1 splitting these into a high and
480 low gain channel for standard mode (2 ADC channels) and combining these for pairs of H and V in polarimetric
481 mode (4 ADC channels). **Radar Range Resolution is calculated using a radiowave velocity in ice of 168
482 m/microseconds and does not include the effect of the processing on the vertical resolution of the system which
483 is expected to be ~50% greater than the values provided in the table, thus these numbers should be interpreted as

484   the theoretical system performance. Diagrams showing the configurations of the three radar systems are
485   provided in the Supplementary Information (Figures S1-3).

Radar Parameters	BAS-built (1994-2004)	PASIN-1 (2004-15)	PASIN-2 (2015-Present)
Antennae Configuration	8x folded dipole (4 Tx / 4 Rx)*	8x folded dipole (4 Tx / 4 Rx)*	12x folded dipole + 4x belly (12 Tx/Rx / 4 Rx only)
Centre Frequency	150 MHz	150 MHz	150 MHz
Transmitted Pulse Width	0.25 µs (pulse) 4 µs linear (chirp)	0.1 µs (pulse) 4 µs linear (chirp)	1 µs (Tukey envelope chirp) 4 µs linear (Tukey envelope chirp)
Chirp Bandwidth	4 MHz (pulse) 10 MHz (chirp)	10 MHz	13 MHz
Antenna Gain	11 dBi	11 dBi	11 dBi
PRF / PRI	20,000 Hz (PRI: 50 µs)	15,635 Hz (PRI: 64 µs)	15,635 Hz (PRI: 64 µs)
Peak Transmit Power	300 W / antennae (1.2 kW total)	1 kW / antennae (4 kW total)	1 kW / antennae (8 kW total)
Receiver SF	25 MHz (scope max single shot)	88 MHz	120 MHz
Receiver FPGA decimation	-	4	-
Receiver Effective SF	25 MHz (SI: 40.0 ns)	22 MHz (SI: 45.5 ns)	120 MHz (SI: 8.3 ns)
Receiver Trace Stacking	64	25 (standard) 50 (polarimetric)	25
Effective PRF (post-stacking)	312.5 Hz	312.5 Hz (standard 2 waveforms)	125.1 Hz (5 waveforms) 208.5 Hz (3 waveforms)
ADC Resolution	12-bit	14-bit	16-bit
Equivalent Sustained Data Rate per ADCs (FPGA)	100 MB/s	176 MB/s (standard) 352 MB/s (polarimetric)	960 MB/s (system: 2.88 GB/s)
Average Data Storage Rate for Full PRI	~1 MB/s	11 MB/s (maximum)	173 MB/s (all arrays)
Radar Range Resolution**	21.0 m (pulse) 8.4 m (chirp)	8.4 m	6.5 m

486

487   The pulse repetition frequency of the PASIN system is 15,635 Hz and hardware stacking is
488   typically set to 25 in standard mode, which results in an effective pulse-coded waveform acquisition
489   rate of 312.5 Hz for each transmit pulse (Table 2). The sample period is 64 µS and the peak
490   transmitted power of the radar system is 4 kW for PASIN-1 and up to 8 kW of possible power for
491   PASIN-2 (1 kW through each transmitting antenna), or 66 dBm. Following stacking, the final
492   sampling frequency of PASIN-1 is 22 MHz and PASIN-2 is 120 MHz (Table 2).

493   **3.1.4 GPS and lidar**

494   Since 1978, navigation has transitioned from basic aircraft data, imagery, and dead reckoning
495   to more modern means, including the use of carrier-phase Global Positioning System (GPS) systems.

496   Between 1994 and 2004, the BAS Twin Otter aircraft was equipped with a Trimble GPS
497   system (1994-95 surveys: Timble 4000SSE; 1996-2003 surveys: Timble 4000SSI). Since 2004, the

498 aircraft is equipped with two, 10-Hz GPS receivers (Leica 500 and ASHTEC Z12 for 2004-18
499 surveys; Javad Delta and Novatel Span for post-2018 surveys) installed on board the aircraft. On the
500 ground, two Leica 500 GPS base stations (replaced by Javad TRIUMPH-2 for post-2018 surveys) are
501 positioned and equipped with choke-ring antennas set up specifically to obtain an unobstructed view
502 of the sky above. Aircraft turns are typically limited to 10-degree banking angles in order to avoid
503 losing connection with the receivers on the ground. The estimated accuracy of the absolute position of
504 the aircraft is 10 cm or less, with the relative accuracy approximately one order of magnitude better.
505 Since 2010, the aircraft altitude and inertial information has been provided by an iMAR FSAS inertial
506 measurement unit (IMU), with the data logged on a Novatel Span receiver. Additional attitude
507 information from the strapdown gravity system is also available for post processing of other datasets.

508 For all modern surveys, the aircraft was also equipped with a Riegl Q240i-80 laser altimeter
509 system (or lidar) in the floor camera hatch to accurately detect the ice surface. The lidar data used for
510 correction of the radar data are typically extracted from the nadir point value with no correction for
511 aircraft altitude. The system has a repetition frequency up to 2 kHz which results in an along-track
512 measurement every 3 cm with an accuracy of up to 5 cm. The lidar is used up to altitudes of 700 m
513 and is constrained by cloud/fog-free conditions.

514 3.2. Data Processing

515 3.2.1 Gravity

516 The raw aerogravity data are processed to obtain levelled free-air gravity anomalies.
517 Although additional survey-specific processing might have been applied to the data, general
518 processing steps for the LaCoste and Romberg system include the calculation of the observed gravity
519 and a range of corrections and filtering functions as described in Jordan et al. (2007; 2010) and
520 Valliant (1992). In particular, corrections for vertical acceleration, Eotvos horizontal motion (Harlan,
521 1968), latitude (Moritz, 1980), and free air (Hackney and Featherstone, 2003) were applied to obtain
522 the final free-air anomalies before subsequent 9-12 km low-pass filtering. As the free-air values refer
523 to the WGS84 ellipsoid, they are defined in geodesy as gravity disturbance.

524 The strapdown gravity method adopted from 2015-onwards directly combined observations
525 of acceleration in all three axes, with orientation and GPS observations combined in a Kalman filter to
526 solve simultaneously for aircraft position and variations in Earth's gravitational field (Becker et al.,
527 2015). For subsequent strapdown-acquisition surveys, some amount of levelling/correction for
528 thermal drift are required. Spectral analysis suggests that the strapdown system can resolve
529 wavelengths on the order of ~5 km (Jordan et al., 2020). Error estimates for the gravity data can be
530 found in the respective survey metadata (see Table 3), or in specific studies utilising the BAS
531 aerogravity data (e.g. Ferraccioli et al., 2006; Forsberg et al., 2018; Jordan and Becker, 2018).

532 Additional processing has, at times, been applied, including the use of masks to remove
533 aircraft turns, start and end of lines, and other regions of noisy data, or producing an upward
534 continued free-air anomaly by upward continuing each line segment from the collected flight altitude
535 to the highest altitude in the survey. The first level of free-air anomaly for all published BAS data is
536 shown in Figure 2a, although it is worth noting that no correction such as downward continuation has
537 been applied to compile the data shown in Figure 2a. It is considered that at the scale of the map, the
538 vertical gradient of residual gravity anomalies at flight altitude is inferior to 2 mGal. Additionally, as
539 the gravity surveys are acquired over the ice sheet, the distance to the bedrock is not only dependent
540 on the flight altitude but also on the ice thickness.

541 3.2.2. Magnetics

542 The raw aeromagnetic data have been processed using the SCAR ADMAP2 data-release
543 protocols (Golynsky et al., 2018). Data were collected at 10 Hz, allowing for modelling and removal

544   of aircraft dynamic movements using a so-called compensation correction (Ferraccioli, et al. 2007).
545   This correction typically requires a dedicated calibration flight in the direction of the survey lines and
546   tie-lines to have been flown. For some surveys with radial design, or where magnetic-data acquisition
547   was opportunistic, logistical constraints meant no calibration flight could be conducted. In these cases,
548   the generally large depth-to-source due to the thick ice allowed for a 10- to 15-second filter to be
549   applied to minimise noise generated by aircraft motion without compromising the geological signal.
550   Given the redundancy of collecting 10 Hz (~6 m spaced) observations over thick ice, most surveys
551   were down-sampled to 1 Hz (~60 m) prior to further processing.

552   After magnetic compensation, the magnetic data were corrected for the International
553   Geomagnetic Reference Field (IGRF), which is a standard mathematical description of the Earth's
554   main magnetic field. Data impacted by operation of aircraft systems such as pumps and heaters were
555   manually determined. Typically such data were discarded, but survey design and lack of alternative
556   data sources mean that sometimes important signatures may be present. In some cases the
557   contaminated data were therefore corrected using an offset correction, accepting that the data segment
558   may be more noisy.

559   The data were then corrected for diurnal variations in the magnetic field using observations at
560   a fixed base station, typically filtered with a 30-minute filter to remove short-wavelength noises
561   potentially not seen on the aircraft. Further statistical levelling of the data based on internal
562   intersections and crossovers with previous surveys was carried out at times to remove systematic
563   errors associated with flight direction (i.e. heading corrections) and additional long-wavelength errors
564   associated with incomplete removal of diurnal variations. In some cases, continuation to a fixed
565   altitude above the ice-sheet bed and a final grid-based micro-levelling procedure was applied
566   (Ferraccioli et al. 1998). The magnetic anomaly map shown in Figure 2b provides an insight of the
567   data coverage and magnitude of magnetic data available. Errors in the data are typically presented as
568   the standard deviation of the crossover errors and can be found in the respective survey metadata (see
569   Table 3).

570   3.2.3. Radar

571   All data acquired with the earlier "BAS-built" radar system (1994-2004) were read using a C
572   code software to convert the LeCroy data to formats readable by Halliburton Landmark's seismic-
573   processing software SeisSpace ProMAX, hereafter just referred as ProMAX. Basic processing was
574   applied to the data in the hardware analogue domain and later using ProMax, including power
575   normalisation and final SEG-Y export. Following the transition from the LeCroy oscilloscope to ADC
576   cards on the "BAS-built" system (see Sect. 3.1.3), MATLAB replaced the IDL language for data
577   processing.

578   As opposed to the "BAS-built" system which, by design, had some level of processing done
579   on the raw data internally, the PASIN system is designed to retain much of the sampled data in the
580   rawest form possible to allow for evolving processing techniques to be applied to the data in the
581   future. For all PASIN data (2004-onwards), the first high-level step was to extract the raw data from
582   the tape drives, convert the three-byte values to conventional four-byte integers, combine the
583   waveforms associated with each pulse transmit type, and then export the data into MATLAB-
584   formatted binary files. Following on from this first step, a chirp-decompression technique using a
585   Blackman window to minimise sidelobe levels was applied using a custom-built MATLAB toolbox,
586   resulting in a processing gain of ~10 decibels (dB).

587   The next step was to apply processing techniques both to enhance along-track resolution and
588   improve the signal-to-noise ratio. For the 2004-05 BBAS survey, incoherent stacking of 10
589   consecutive traces was applied and a moving-average window filter used, however no Synthetic
590   Aperture Radar (SAR) techniques were applied to these data. First tested on previously acquired

591 PASIN radar data (Hélière et al., 2007), 2-D SAR processing based on the Omega-K algorithm and
592 subsequently improved versions using Doppler-beam sharpening were applied systematically to all
593 the deep-sounding chirp data from 2005-2006 onwards to increase spatial resolution and remove
594 backscattering hyperbolae in the along-track direction (Corr et al., 2007; Jeofry et al., 2018). The
595 benefit of using unfocused along-track SAR processing is that it resolves the bed in much finer detail
596 compared with non-SAR focused data (see Fig. 6 b-c); however SAR-processing can also lead to
597 distortions of the amplitude of the ice structure and bed reflection in unhomogenous areas of the ice
598 sheet (e.g. near grounding line; see Hélière et al., 2007) and thus might not always be appropriate for
599 assessing internal layering or absolute amplitudes such as required for bed-reflectivity analysis.
600 Additional moving-average filters of varying lengths have also been applied to enhance englacial
601 reflections and improve visualisation of the radar data.

602 Figure 6 shows the three processed radar products provided for the 2010-11 IMAFI survey
603 over West Antarctica, with Figure 6a showing the shallow-sounding pulse, and Figure 6b-c the deep-
604 sounding chirp radar data using the unfocused SAR-processing technique from Hélière et al. (2007)
605 (Fig. 6b) and a version of the chirp product processed with coherent summations but with no SAR-
606 processing applied (Fig. 6c). Internal layering is more clearly visible in the upper part of the ice
607 column on the pulse data compared with the chirp data (see black-bordered insets in Fig. 6a and 6c),
608 however deeper internal layering is much more visible on the SAR-chirp than the non-SAR chirp
609 (Fig. 6b-c). Additionally, the peak amplitude of the bed is better resolved in the SAR-processed chirp
610 than the non SAR-processed chirp (see white-bordered inset in Fig. 6b-c).

611
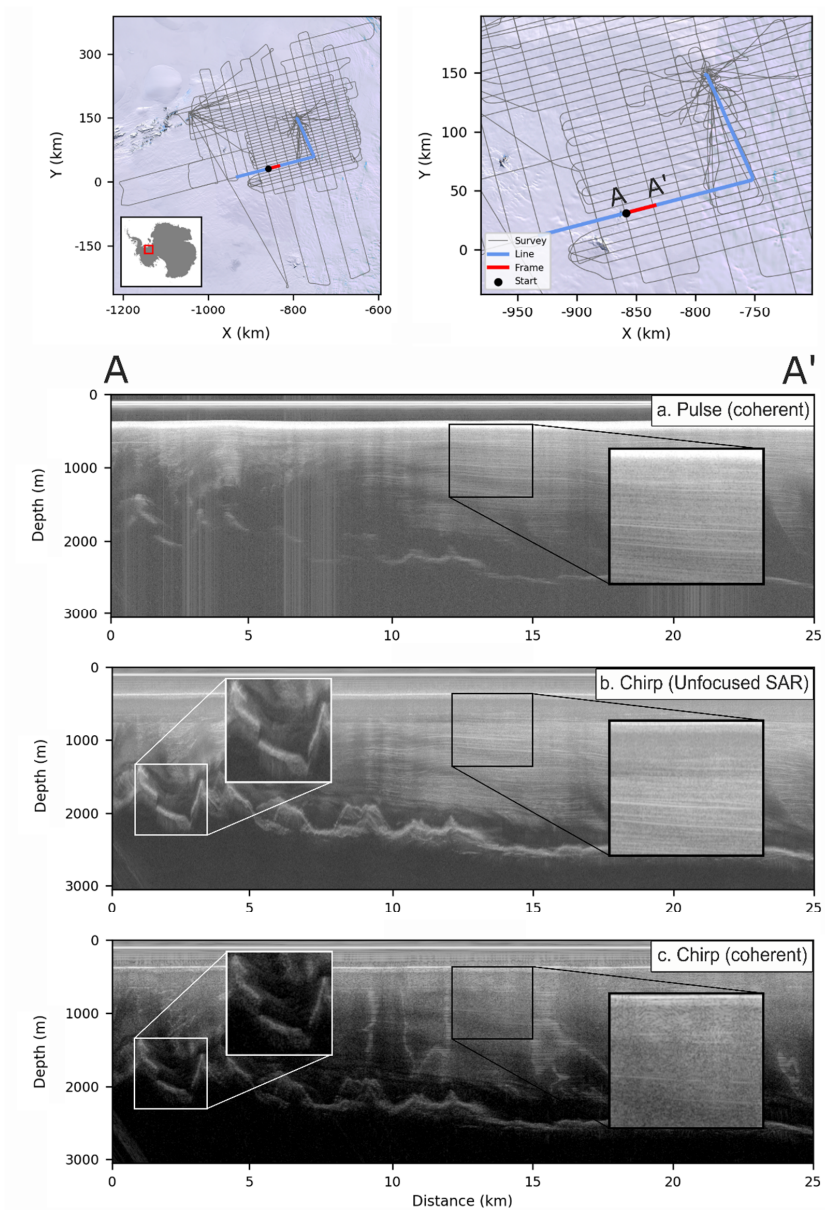
Figure 6. A 25-km segment for flightline 15d of the 2010-11 IMAFI survey showing the three radar products and processing attributes. The top two panels show an overview map of the entire survey with an inset over Antarctica and a zoomed-in map over the specific flightline with the 25-km radar segment (defined as A-A') shown in red. The background satellite image in the upper two maps is from the Landsat Image Mosaic of Antarctica (LIMA) (Bindschadler et al., 2008). The bottom three radargrams show a 25-km segment of the data for the three products provided for the 2010-11 IMAFI survey as follows: (a) the coherently processed, shallow-sounding pulse, (b) the unfocused 2-D SAR-processed, deep-sounding chirp, and (c) the coherently processed, deep-sounding chirp. The black-bordered insets zoom to the internal layering in the upper portion of the ice column for the three radar products and the white-bordered insets show the difference in bed characteristics between the two processed chirp products.

622   Note that further processing of the PASIN data has also been applied by others using simple
623 image-processing techniques such as moving-average filters to enhance the internal layering of the ice
624 and reduce incoherent noise (Ashmore et al., 2020; Bodart et al., 2021), or by applying more complex
625 SAR processing techniques such as over previously incoherently processed radar data (Chu et al.,
626 2021). Additional techniques have also be employed in areas where side-echos from steep valley
627 walls lead to ambiguous bed reflections and thus may affect ice thickness estimates, as previously
628 employed over Flask Glacier (Antarctic Peninsula) using PASIN SAR-processed data and a
629 combination of velocity and digital elevation models to obtain more accurate ice thickness estimates
630 (Farinotti et al., 2013).

631   Following on from the processing of the radar data, the last step was to "pick" the bed and
632 ice-surface reflectors. It is worth stating that picking the onset of the basal echo (i.e. where the echo
633 amplitude is greater than the noise floor) as done on the BAS data is not a universal method applied
634 by all institutes, who, may pick the half-amplitude delay or the peak value, leading in turn to
635 measurement biases across institutes and data products (e.g. Chu et al., 2021; Peters et al., 2005).

636   We picked the bed in ProMax, using a semi-automatic first-break pick algorithm on the chirp
637 data below a top-mute window (generally ~100 samples above the bed reflection) to locate the precise
638 bed return. This was followed by manual checks and re-picking to exclude any unrealistic spikes. In
639 areas where multiple closely spaced reflectors were sounded at the bed, the shallowest reflection was
640 assumed to be the bed as off-axis reflectors would likely appear lower down in this section. However,
641 in some cases, reflectors which appeared deeper were chosen, with shallower weak reflectors assumed
642 to reflect entrained debris, accreted ice, or uncompensated refraction hyperbolae close to the bed.

643   Since the PASIN system does not resolve the ice surface well due to errors in the phase centre
644 of the pulse in reflections from the firn layer, the surface reflector as imaged by the radar was only
645 rarely used on its own to calculate the actual ice surface location on the radargrams. However, to
646 estimate ice thickness and hence correct for bed elevation, the location of the surface reflector in the
647 radargram must be known accurately. Thus, range-to-surface from coincident on board-acquired lidar,
648 or alternatively if lidar was not available (i.e., due to clouds or ground clearance higher than 750 m),
649 using surface elevation from an accurate Digital Elevation Model (DEM) (i.e. REMA 8-m DEM for
650 latest surveys; Howat et al., 2019), was used to calculate the "theoretical" surface pick, as follows:

651   Firstly, the same semi-automatic picker used for picking the bed was used on a subset of the
652 shallow-sounding pulse data with a bottom-mute window set at ~100 samples below the surface
653 reflection. Secondly, once aircraft-to-surface range was obtained from lidar, a linear trend between the
654 surface pick from the radar and the surface range from the lidar was calculated, and a resulting slope
655 and offset was used to calculate the theoretical location of the surface. Where possible, the range-to-
656 ground value was derived from the lidar data or interpolated from the mean lidar elevation within
657 ~700 m. In those rare cases where the surface reflection was picked directly from the radar, a
658 regression, local to the data gap, was used to fit the radar range to terrain clearance. For older surveys
659 where on board lidar or accurate DEMs were not available to calculate range-to-ground, the height of
660 the aircraft above the surface was obtained by the aircraft's radar altimeter which was then converted
661 into a radar delay time. This conversion was done after a two-stage calibration process which
662 involved recording the terrain clearance over a sea surface with the two instruments, and then
663 correction for the penetration depth of the radar altimeter was obtained from the difference in the
664 height above ellipsoid of a surveyed 'flat' snow surface and the aircraft. Where possible, the reference
665 surface was chosen to be in the centre of the targeted area.

666   Once bed and surface reflectors were picked, ice thickness was obtained by calculating the
667 difference between the bed and surface pick in range samples (relative to the BAS system). The
668 picked travel time was then converted to depth in metres using a radar wave speed of 168
669 m/microseconds and a constant firn correction of 10 m. Bed and surface elevations were then

670   integrated with a high-precision kinematic dual-frequency GPS position solution to provide the final
671   point dataset of elevations relative to the WGS84 Ellipsoid. To ensure best accuracy of satellite-orbit
672   definitions and atmospheric corrections, the interpolated survey locations and aircraft elevations were
673   processed from 10-Hz coupled Precise Point Positioning (PPP) GNSS/INS solutions one month after
674   data acquisition. Measurement errors were typically calculated from crossover analysis for an entire
675   survey using the root-mean-square deviation of the surface, bed and ice thickness at intersection
676   transects, and can be found in the various studies utilising the PASIN data (see Jeoffry et al., 2018;
677   Rose et al., 2013; Ross et al., 2012; Vaughan et al., 2006), or alternatively in the respective survey
678   metadata (see Table 3).

679

4. FAIR Data Publishing

681   In total, we have published 64 datasets from 24 surveys as part of this data release,
682   representing ~566 GB of data and ~1800 files. This amounts to a total of 3.62 million gravity and 7.41
683   million magnetic data points, as well as 14.5 million ice-thickness and bed-elevation measurements.
684   The complete list of published datasets is provided in Table 3, including the short Digital Object
685   Identifiers (DOI) which redirect to the metadata sheets and download folders for each respective
686   dataset archived on the PDC Discovery Metadata System (DMS) data catalogue
687   (https://data.bas.ac.uk/).

688   **Table 3. Short Digital Object Identifiers for the gravity, magnetic, bed-pick, and 2-D radar**
689   **datasets for each survey flown by BAS and included in this data release.** Abbreviations used are the same as
690   in Table 1. The links in this table can also be accessed by adding the short DOI preceded by 'https://doi.org/'.
691   '*'For the PolarGAP survey, data can be downloaded from both the ESA and BAS data catalogues, but the DOI
692   for the gravity and magnetic data (https://doi.org/10.5270/esa-8ffoo3e) belongs to ESA. If using the PDC data
693   catalogue, the PolarGAP gravity and magnetic data can be downloaded from https://data.bas.ac.uk/full-
694   record.php?id=GB/NERC/BAS/PDC/01583 and https://data.bas.ac.uk/full-
695   record.php?id=GB/NERC/BAS/PDC/01584 respectively. '**' indicates that the data are not held at BAS, but
696   instead are available on the CReSIS data portal (https://data.cresis.ku.edu/).

Survey	Year	Region	Gravity	Magnetic	Bed-pick	Radar
EVANS	1994-95	WAIS	10/d549	-	10/d548	-
Black Coast	1996-97	APIS	-	10/d54x	-	-
CHARCOT	1996-97	APIS	-	10/d54z	-	-
JRI	1997-98	APIS	10/d55g	10/d55f	-	-
LARSEN	1997-98	APIS	-	10/d55k	-	-
DUFEK	1998-99	WAIS	10/d546	10/d544	10/d542	-
AFI Coats Land	2001-02	EAIS	-	10/dpnw	10/dpnx	-
MAMOG	2001-02	EAIS	10/dpqg	10/dpqh	10/dpqd	-
TORUS	2001-02	WAIS	10/dpqm	10/dpqj	10/dpqf	-
SPARC	2002-03	APIS	10/d552	10/d55x	-	-
BBAS	2004-05	WAIS	10/dpn6	10/dpn3	10/dpnz	10/gzqs
WISE-ISODYN	2005-06	EAIS	10/d554	10/d553	10/cncc	10/gzqq
GRADES-IMAGE	2006-07	WAIS	-	10/d55d	10/d55c	10/gzqj
AGAP	2007-09	EAIS	10/dpnf	10/dpnn	10/dpnr	10/gzqw
ANDRILL HRAM	2008-09	WAIS	-	10/d54w	-	-
Adelaide Island	2010-11	APIS	-	10/dn8b	-	-
IMAFI	2010-11	WAIS	10/dn8g	10/dn8h	10/dn8f	10/gzqr
PIG Ice Shelf	2010-11	WAIS	-	10/d55m	10/d55n	-
ICEGRAV	2011-13	EAIS	10/dpqb	10/dpp9	10/cjzn	10/gzqt

FISS 2015	2015-16	WAIS	-	10/g36h	10/g35q	10/g35m
PolarGAP 2015	2015-16	EAIS	10/g7kw*	10/g7kw*	10/g7qq	10/g7qp
FISS 2016	2016-17	WAIS	10/g36f	10/g36j	10/g35t	10/g35p
ITGC 2018	2018-20	WAIS	10/dn26	10/dn24	**	**
ITGC 2019	2019-20	WAIS	10/g68r	10/g68q	10/gp4z	10/g7qn

697

698 Below, we discuss the release of the datasets centered around the four FAIR data principles
699 (i.e. Findable, Accessible, Interoperable and Re-Usable; Wilkinson et al., 2016), starting with the
700 formats and attributes used to store and describe the data (Interoperability; Sect. 4.1), the metadata
701 and Digital Object Identifiers assigned to each dataset (Findability; Sect. 4.2), the data-portal
702 infrastructure and functionalities (Accessibility; Sect. 4.3), and finally the creation of a user guide and
703 open-access tutorials written in Python and MATLAB for reading the data programmatically (Re-
704 usability; Sect. 4.4).

705 **4.1. Interoperability: Data Formats and Attributes**

706 In order to make our data as interoperable as possible, the choice of an open format for all our
707 datasets was a priority. We followed the best practices of the geophysics community and used
708 common data formats and naming conventions to describe the variable names. These are detailed
709 further here.

710 The gravity, magnetic, and bed-pick data are stored in open ASCII data formats, namely XYZ
711 and CSV files, to ensure long-term access and unresctricted use of the data in the future (Fig. 4).
712 Additionally, we followed the SCAR ADMAP2 data-release protocols (Golynsky et al., 2018) for the
713 naming convention of the channels for the magnetic data. For the radar data, we chose to release the
714 bed-pick data separately from the full radar data (Fig. 4), although the full radar product contains most
715 of the information stored in the ASCII bed-pick files. Publishing the bed-pick data separately from the
716 radar data was a deliberate choice: it alleviates the need for users to download the full radar datasets
717 to access light-weight tabular data, and improves the accessibility of the point data for large gridded
718 products such as SCAR's BEDMAP (Fretwell et al., 2013) and NASA's BedMachine (Morlighem et
719 al., 2020) projects. The bed-pick data are stored as ASCII-formatted files (namely XYZ and CSV),
720 whereas the full radar data are stored as SEG-Y and NetCDF files, reasons for which are described
721 below.

722 The SEG-Y format has been used extensively by radar scientists since the early 1980s to store
723 radar data. This is primarily due to the lack of a radar-specific format, SEG-Y having been developed
724 primarily to store seismic data. The advantage of using SEG-Y files is that data can be readily
725 imported into seismic-interpretation software for data interpretation and analysis. The drawbacks of
726 using SEG-Y, however, are numerous, making this option unsuitable for long-term data storage.
727 These include: (1) limited space for metadata, (2) the choice of byte-information to store the radar
728 data is subjective due to the nature of the SEG-Y format, (3) until recently, the byte stream structure
729 which includes the geolocation of each radar trace (i.e. the X and Y positions) was restricted to integer
730 format leading to large inaccuracies in the actual trace position despite the use of high-resolution, sub-
731 metre GPS data (see Sect. 3.1.4). Recognising, however, the need from the geophysical community to
732 view and analyse the radar data in conventional data formats, we have decided to continue producing
733 SEG-Y files for each flightline and acquisition mode (e.g. pulse and chirp). The SEG-Y files were
734 produced using the Revision 1.0 SEG-Y format and georeferenced using the navigational position of
735 each trace from the GPS on board the aircraft in Polar Stereographic (EPSG: 3031) projection. Each
736 SEG-Y file contains the following byte-information: trace number (byte: 1-4 and 5-8), PRI-Number
737 (byte: 9-12), Cartesian X-coordinate (byte: 73-76), Cartesian Y-coordinate (byte: 77-80), number of
738 samples for each SEG-Y trace (byte: 115-116), and the sampling interval (byte: 117-118).
739   As a result of the issues mentioned above, we also exported the radar data in NetCDF-
740 formatted files. We chose the NetCDF format due to its portability and array-oriented structure, the
741 ability to store large amounts of metadata and variables into one portable file, its machine-readable
742 capability, and to harmonise our data products with other fields such as climate science (e.g. ECMWF
743 ERA5 reanalysis products; NCAR climate data), glaciology (e.g. Lei et al., 2021; Le Brocq et al.,
744 2010; Morlighem et al., 2017) and, increasingly, radar geophysics itself (e.g. Blankenship et al., 2017;
745 Paden et al., 2014), which already all make use of this data format effectively. The NetCDF files we
746 produced contain extensive metadata relating to the acquisition and processing of the radar data, as
747 well as a set of CF-compliant (Climate and Forecast; https://cfconventions.org/) variables that are tied
748 to the radar data (Table 4). As a minimum, each NetCDF file contains a radar data variable (one for
749 the pulse and/or one for the chirp if both exist) in 2-D format, and a set of 1-D variables relating
750 directly to the radar data, such as the trace number, PRI number, fast time, and the X and Y
751 coordinates (Table 4). We also provided additional radar-related variables which were extracted from
752 the radar data following processing, such as the surface and bed picks, the surface and bed elevation,
753 the ice thickness, longitude and latitude, time of the trace, and the elevation of the aircraft (Table 4).
754 Additional 1-D variables include the source of the surface pick (from lidar or radar) if this exists, the
755 range between the aircraft and the ice surface, and in case the pulse- and chirp-radar variables do not
756 have the same length, we provide two sets of variables for the trace number and PRI number.

757   **Table 4. Attributes for each variable stored in the NetCDF files.** For each attribute name, we
758 provide the long name, the dimension (1- or 2-D, x- or y-axis), the short or CF-compliant standard name, and
759 the unit of the measurement. The standard name is only provided if it exists as part of the CF convention
760 (https://cfconventions.org/), otherwise a short name is provided. "dBm" stands for decibel-milliwatts and "a.s.l."
761 stands for above sea level. Note that the surface and bed pick data are referenced to the sampling time of the
762 BAS radar systems across the 64 microseconds pulse repetition interval window, and digitised according to the
763 receiver sampling frequency (see Table 2).

NetCDF Attributes	Long Name	Dimension	Short / Standard Name	Unit
traces	Trace number for the radar data	1-D (x-axis)	traceNum	integer count (unitless)
fast_time	Two-way travel time	1-D (y-axis)	time	microseconds
x_coordinates	Cartesian x-coordinates for the radar data	1-D (x-axis)	projection_x_coordinate	meters (WGS84 EPSG: 3031)
y_coordinates	Cartesian y-coordinates for the radar data	1-D (x-axis)	projection_y_coordinate	meters (WGS84 EPSG: 3031)
chirp_data	Radar data for the processed chirp	2-D (x- and y-axis)	-	power (dBm)
pulse_data	Radar data for the processed pulse	2-D (x- and y-axis)	-	power (dBm)
longitude_layerData	Longitudinal position of the trace number	1-D (x-axis)	longitude	degree_east (WGS84 EPSG: 4326)
latitude_layerData	Latitudinal position of the trace number	1-D (x-axis)	latitude	degree_north (WGS84 EPSG: 4326)
UTC_time_layerData	Coordinated Universal Time (UTC) of trace number	1-D (x-axis)	resTime	seconds of the day

PriNumber_layerData	Incremental integer reference number related to initialisation of the radar system	1-D (x-axis)	PriNum	integer count (unitless)
terrainClearance_layerData	Terrain clearance distance from platform to air interface with ice, sea or ground	1-D (x-axis)	resHt	meters
aircraft_altitude_layerData	Aircraft altitude	1-D (x-axis)	Eht	meters a.s.l. (WGS84 ellipsoid)
surface_altitude_layerData	Ice surface elevation for the trace number	1-D (x-axis)	surface_altitude	meters a.s.l. (WGS84 ellipsoid)
surface_pick_layerData	Location down trace of surface pick (BAS system)	1-D (x-axis)	surfPickLoc	time sample (microseconds)
bed_altitude_layerData	Bedrock elevation for the trace number	1-D (x-axis)	bed_altitude	meters a.s.l. (WGS84 ellipsoid)
bed_pick_layerData	Location down trace of bed pick (BAS system)	1-D (x-axis)	bedPickLoc	time sample (microseconds)
land_ice_thickness_layerData	Ice thickness for the trace number	1-D (x-axis)	land_ice_thickness	meters

764

765   Lastly, to aid visualisation and improve efficiency in navigating the datasets, we created
766 lightweight quick-look PDF files of the radar data for each flightline of each survey (Fig. 7). Each
767 quicklook file contains three plots: an overview map of the specific survey with an inset of its position
768 over Antarctica and the specific flightline highlighted in blue (Fig. 7a), a closer zoomed-in version of
769 the specific flightline with the frame footprint and start point for the segmented radargram shown as a
770 red line and black dot respectively (Fig. 7b), and the segmented ~25 or ~50-km segment shown in
771 Figure 7b as a 2-D radargram of the chirp radar data, with the surface and bed pick shown as a red and
772 blue dashed lines respectively (Fig. 7c). The x-axes in Figure 7c show the trace number (top) and
773 distance in kilometers (bottom) respectively. The choice of ~25 or ~50-km length for the 2-D
774 radargram was chosen based on clarity of the image and varies from survey to survey. The quick-look
775 PDF files are stored alongside the SEG-Y and NetCDF files and are accessible using the links
776 provided in Table 3.

777
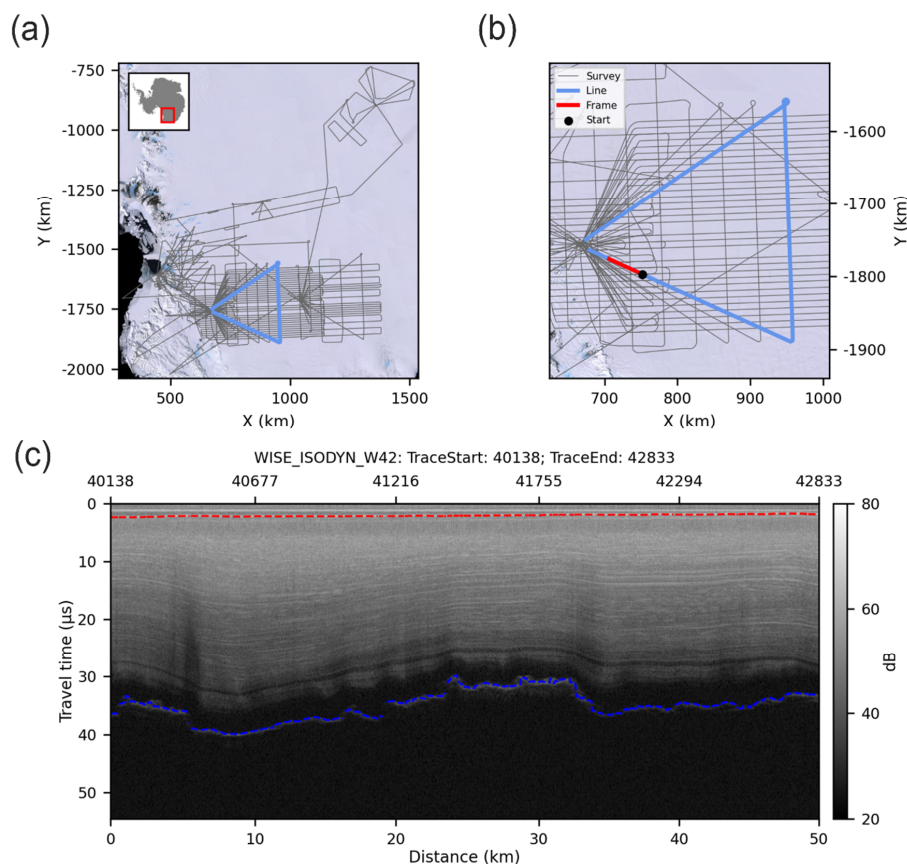
Figure 7. Example of a segmented quick-look image from the 2005-06 WISE-ISODYN survey. (a) Overview map of the entire survey with an inset over Antarctica. (b) Zoom to version to which the segment belongs with the frame footprint and start point for the radargram shown. The background satellite image in (a-b) is from the Landsat Image Mosaic of Antarctica (LIMA) (Bindschadler et al., 2008). (c) 50-km segmented radar image of the chirp data with distance in kilometres shown in the bottom x-axis and the trace number shown in the top x-axis. The format of the title in (c) is as follows: Survey Name and Flight ID, First Trace of Segment, Last Trace of Segment. The red and blue dashed lines on the radargram (c) are the surface and bed pick respectively.

4.2. Findability: Metadata and Digital Object Identifiers

ISO 19115/19139 Geographic Information metadata are provided for each data type of each survey and is archived alongside the datasets onto the PDC DMS catalogue (https://data.bas.ac.uk/; see Table 3). Each metadata record provides detailed information about the dataset, including an abstract, list of personnel involved in the acquisition or analysis of the dataset, and detailed lineage information on the acquisition and processing steps used to produce the dataset amongst others. All our data are covered under the UK Open Government License (http://www.nationalarchives.gov.uk/doc/open-government-licence/), enabling the re-use of the data freely and with flexibility, whilst at the same time ensuring acknowledgment of those involved in the collection and processing of the data. In addition, we use Earth Science-specific keywords and vocabularies from the Global Change Master Directory (GCMD, 2021) to describe our data in a

797   consistent and comprehensive manner in accordance with ISO 19115 standards. Lastly, a Digital
798   Object Identifier is minted for each dataset so that it can be discoverable and adequately cited. The
799   end goal is to provide all the information necessary for effective, long-term data re-use.

800   The data are shared via the web-based RAMADDA (Repository for Archiving and MAnaging
801   Diverse DAta; https://geodesystems.com/) data repository system which is an open-source content
802   and data management platform. The download of the data is done through a standard HTTP-protocol
803   where no login account is required. In the backend, the data are stored following a simple folder
804   structure on the PDC server that is mirrored onto RAMADDA. This simple structure allows us to
805   maintain a balance between the services we can provide and our ability to move away from specific
806   tools – RAMADDA in this case - and potentially adopt more performant systems in the future. The
807   goal is to stay as independent of the platform we use as possible while providing the most effective
808   service possible.

809   **4.3. Accessibility: Polar Airborne Geophysics Data Portal**

810   To increase the accessibility and discoverability of our data, we developed a new data portal,
811   the Polar Airborne Geophysics Data Portal (https://www.bas.ac.uk/project/nagdp/). The portal allows
812   to showcase interactively the wide coverage of aerogeophysical datasets collected by BAS and
813   enables users to easily discover and download the published datasets via a series of widgets and
814   functionalities aimed at enhancing the user experience.

815   The portal is divided into five layer-menus: "Aerogravity", "Aeromagnetics", "AeroRadar",
816   "Boundaries & Features", and "Basemaps". The first three menus contain shapefile layers for the
817   gravity, magnetic, and radar datasets respectively. The "Boundaries & Features" menu contains a set
818   of specific boundary layers, such as the Antarctic Coastline and Ice Drainage boundaries amongst
819   others, and the "Basemaps" menu contains background maps such as ice thickness, surface and bed
820   elevations, magnetic anomaly and geothermal heat flow maps amongst others.

821   The track lines for each dataset correspond to individual polyline shapefiles (either segmented
822   in 25 or 50-km, or by flightline) which contain key statistics such as the minimum, maximum, and
823   median gravity and magnetic anomalies, and minimum, maximum, and median ice surface, bed
824   elevation, and ice thickness. The shapefiles also contain direct links to the survey's metadata and to
825   direct links to download the data via the RAMADDA interface.

826   A powerful functionality of the portal is the ability to view the aerogeophysical data rapidly
827   via the creation of quick-look gravity, magnetic, and radar plots for each flightlines (see Sect. 5.2;
828   Figure 7c). For the magnetic and gravity data, graphs showing the magnetic or free-air anomaly along
829   straight lines were created in the direction Westernmost-Easternmost if the profile is mainly in the
830   direction of the longitude, or Northernmost-Southernmost if the profile is predominantly in the
831   direction of the latitude. For the radar data, the segmented images were produced in a similar format
832   to Figure 7c and split into ~25 and~50 km segments depending on the survey.

833

4.4. Re-Usability: User Guide and Tutorials

To increase further the re-usability of our data, we provided a user guide for the data portal as well as interactive, open-source Jupyter Notebook tutorials written in Python and MATLAB for reading in the gravity, magnetic, and radar datasets and conducting first-order analyses on the data. These are archived on the BAS GitHub repository and provided via an interactive web interface using Jupyter Book (https://antarctica.github.io/PDC_GeophysicsBook). We believe these to be particularly beneficial for ensuring accessibility and re-usability of our data to as wide of a range of users as possible, primarily as a result of the complexity around reading in aerogeophysical data formats. Section 5.1 discusses further the potential re-usability of the radar data.

5. Discussion

This final section exemplifies the potential re-usability of the newly released radar data via the interrogation of the englacial architecture of the ice as sounded by BAS ice-penetrating radars. We also explore the future use of the new data portal and discuss opportunities in terms of data release and further potential re-use of the BAS aerogeophysical data.

5.1. Internal Layering Continuity Index

Englacial layering, as imaged by ice-penetrating radars, is a powerful means of extracting information on past ice-dynamical processes (Bingham et al., 2015; Siegert et al., 2003) amongst others. For example, the presence of well-preserved and continuous englacial layering may reflect stable ice conditions and suggest changes in past ice-flow conditions, ice divide migration, or melting within or at the base of an ice sheet are limited (Karlsson et al., 2012). In contrast, poor continuity in englacial layering, primarily characterised by buckled or absent layering, may be indicative of past ice-flow switching or increased englacial stress gradients (Bingham et al., 2015; Siegert et al., 2003). Thus, quantifying the continuity of englacial layering is essential in our understanding of past and current ice dynamical conditions, and can also be used for selecting ice-core drilling sites (Karlsson et al., 2018), or to identify areas which could benefit from being re-surveyed in more detail with more modern systems or acquisition strategies.

Several methods have been developed for mapping the continuity of englacial layering from ice-penetrating radar data (e.g. Delf et al., 2020; Karlsson et al., 2012; Sime et al., 2014). One such technique, the Internal Layer Continuity Index (or ILCI; Karlsson et al., 2012) is the first to provide an automated tool for quantitatively assessing the continuity of englacial layering based on A-scope radar profiles. This method has the advantage of being much less laborious than manual methods (e.g. Bingham et al. 2007; Rippin et al., 2003a; Siegert et al., 2003) and removes the potential subjectivity in assessing layer continuity. Additionally, the large amount of radar data now available precludes the ability to identify layer continuity manually, making the ILCI a powerful tool in our ability to extract this valuable metric. By design, the ILCI is sensitive to the number and strength of internal reflections, such that low values indicate discontinuity and high values indicate high continuity. First tested over selected 2004-05 BBAS flightlines covering the Pine Island Glacier (Karlsson et al., 2012), the ILCI was subsequently employed over Institute and Möller Ice Stream (Bingham et al., 2015; Winter et al., 2015) and East Antarctica (Karlsson et al., 2018; Luo et al., 2020). Using the ILCI previously calculated for the 2010-11 IMAFI radar data, Ashmore et al. (2020) further demonstrated that the ILCI was statistically higher where manually picked internal layers could be traced, thus showing for the first time that this method has the potential to be applied at a larger scale with reliable results. However, until now, this approach had not been tested at a regional scale over Antarctica and with the use of multiple radar datasets.

879 Here, we have calculated the ILCI on the ten PASIN radar datasets that have been published
880 as part of this data release (Fig. 8-9). This includes a total of ~300,00 line-km of 2-D radar data from
881 the BBAS-AGASEA (2004-05), WISE-ISODYN (2005-06), GRADES-IMAGE (2006-07), AGAP
882 (2007-09), IMAFI (2010-11), ICEGRAV (2012-13), FISS (2015-17), PolarGAP (2015-16), and ITGC
883 Thwaites (2019-20) surveys (see Table 3). Since we were primarily interested in regional changes in
884 layer continuity, the ILCI was smoothed using a horizontal window of 1000 samples (representing
885 ~25-45 km distance depending on the dataset) to remove any small-scale anomalies in the data and
886 only making use of the deep-sounding chirp product due to its capability of imaging deeper internal
887 layers. The upper and lower 20% of the ice were also omitted in the calculations to avoid surface
888 noise affecting the result in the upper part of the ice column, and because internal layering is typically
889 absent near the ice-bed interface (Karlsson et al., 2012).

890
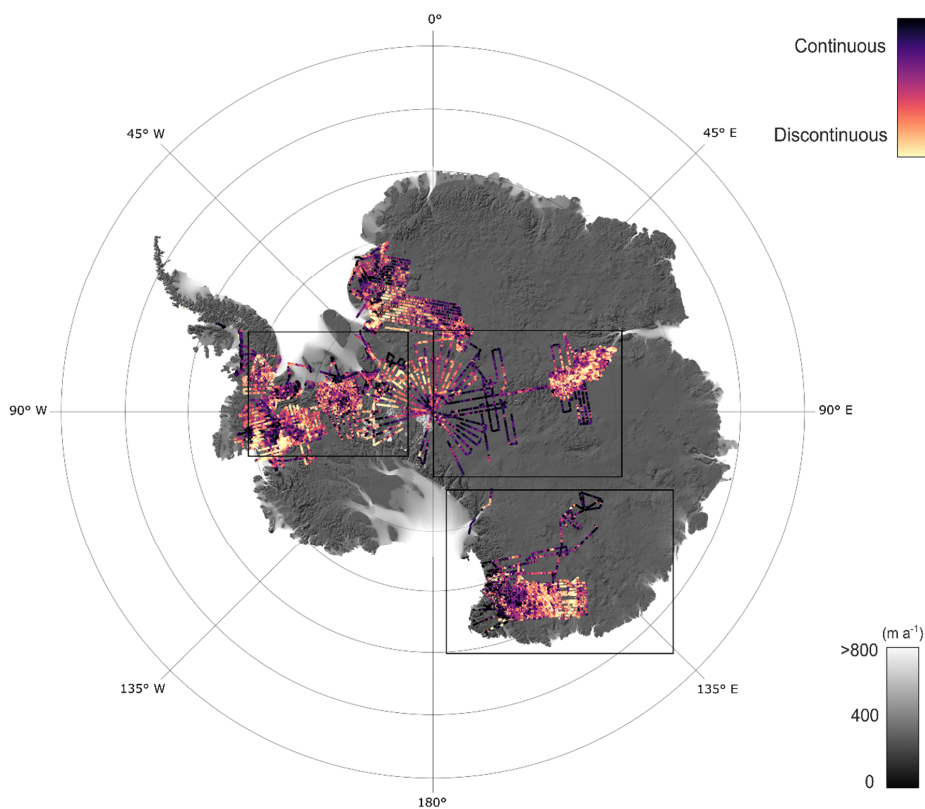
891

892 **Figure 8. Internal Layer Continuity Index for the ten PASIN datasets for which the fully**
893 **processed 2-D radar data was released as part of this paper (see Table 3).** The background map shows ice-
894 flow velocities from the In-SAR MEaSUREs dataset (Rignot et al., 2017) superimposed over a hill-shade from
895 the BedMachine bed elevation dataset (Morlighem et al., 2020). The black and white colour bar shows ice-flow
896 velocities in metres per annum, and the magma colour bar shows the continuity of internal layers throughout the
897 radar dataset (low ILCI values = yellow; high ILCI values = dark purple). The black-bordered rectangles are
898 shown in more detail in Figure 9a-c.

899 An important consideration in employing the ILCI over multiple datasets is that the results
900 will vary based on data acquisition (i.e. radar frequency, system resolution) and processing applied
901 (i.e. incoherent vs 2-D SAR), thus a pan-Antarctic comparison of internal layer continuity must be

902 analysed in this context. This is especially the case here, where we have applied the ILCI to data
903 acquired over a period of >15 years with two different systems (namely PASIN-1 and PASIN-2) and
904 using different processing regimes. Therefore, care must be taken when interpreting the results from
905 different surveys together, as for example, a low level of layer continuity in the main trunk of Pine
906 Island Glacier on the BBAS survey may not reflect the same level of discontinuity on the low-
907 continuity areas of the AGAP survey. This caution noted, the results presented here offer an
908 opportunity to identify some regional patterns of potential value for future work, as we now discuss.

909 Figure 8 shows that there is a good correspondence between discontinuous layering where ice
910 flow is fast (> 200 m a^{-1}) such as over Foundation Ice Stream (FISS) and the main trunk of Pine Island
911 Glacier (BBAS) and Slessor Glacier (ICEGRAV) (Fig. 8 and 9a). Whilst layer discontinuity is mainly
912 present over the WAIS due to the high concentration of fast-flowing ice streams in this region, several
913 sections covering the EAIS also show signs of layer discontinuity, particularly in the upstream
914 portions of the fast-flowing Lambert Glacier (AGAP), as well as over David and Ninnis glaciers
915 (WISE-ISODYN) (yellow arrows in Fig. 9b-c).

916 Unsurprisingly, areas of high continuity are mainly observed over the interior of the EAIS,
917 particularly on flightlines extending deep into East Antarctica and South Pole (Fig. 8 and 9a-b), as
918 well as into the deeper parts of the Wilkes Subglacial Basin and Dome C where deep ice-cores have
919 been drilled (black arrow in Fig. 9c). Areas of high layer continuity over the WAIS include numerous
920 ice-rises (i.e. Bungenstock, Fletcher, Henry, and Skytrain) as imaged on the GRADES-IMAGE and
921 FISS surveys (black arrows in Fig. 9a), the deeper sections of the southern Pine Island Glacier basin
922 on the BBAS data, as well as on PolarGAP survey lines upstream of the FISS grids covering
923 Foundation Ice Stream (Fig. 9a).

924 Also visible are the disruptive effects of local bed topography on the continuity of internal
925 layering, such as over the Ellsworth Subglacial Mountains (BBAS) and at the onset of the Pensacola
926 and Transantarctic Mountains as seen on the IMAFI and PolarGAP survey flightlines (yellow arrows
927 in Fig. 9a), with relatively flat bed topography in the deep interior of the EAIS allowing layering to
928 remain relatively undisturbed (Fig. 8 and black arrows in Fig. 9b).
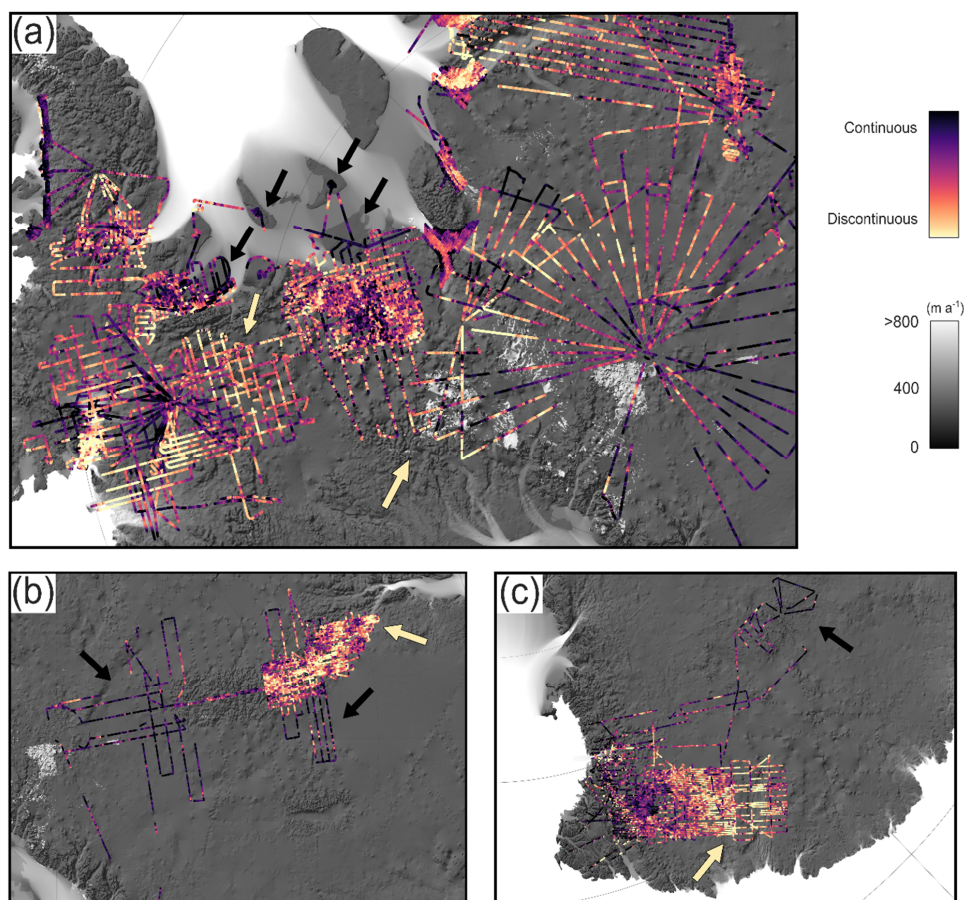
929
930   **Figure 9. Zoomed-in sections of the Internal Layer Continuity Index shown in the black-**
931   **bordered rectangles on Figure 8.** The basemap datasets and colour scales are the same as in Figure 8. (a) ILCI
932   results over the WAIS (including Pine Island Glacier, Rutford Ice Stream, Institute-Möller Ice Stream, and
933   Foundation Ice Stream) and bottleneck with the EAIS (including South Pole, Pensacola Mountains and Slessor
934   Glacier), (b) ILCI results for the AGAP survey over East Antarctica's Dome A and South Pole, (c) ILCI results
935   for the WISE-ISODYN survey over East Antarctica's Wilkes Subglacial Basin and Dome C. Arrows refer to
936   locations mentioned in the text, with black arrows highlighting examples of high layer continuity and yellow
937   arrows low layer continuity.

938   Altogether, the results presented in Figures 8 and 9 show the potential for the yet-unexplored
939   radar datasets to be further exploited in the future, particularly with regards to tracking or otherwise
940   characterising the englacial architecture of the ice and as motivated by the SCAR AntArchitecture
941   group. At present, only two BAS radar datasets (BBAS and IMAFI) have been comprehensively
942   assessed for deep englacial layers (Ashmore et al., 2020; Bodart et al., 2021; Karlsson et al., 2009).
943   Thus, the release here of large swaths of additional radar datasets, including over the more stable
944   regions of the EAIS (namely the AGAP, ICEGRAV, PolarGAP, and WISE-ISODYN datasets), and
945   the evidence indicated here by the ILCI of large regions of continuous englacial layering in the region
946   will likely offer more promising opportunities for englacial work to be conducted on these datasets. In
947   particular, the close proximity of deep ice cores to the ITGC Thwaites surveys (i.e. WAIS Divide ice-
948   core; Buizert et al., 2015 and Sigl et al., 2016) and the WISE-ISODYN survey (i.e. EPICA Dome C
949   ice-core; EPICA Community Members, 2004) provide ready opportunities for these layers to be

950 dated, increasing significantly their use for wider applications such as estimating past accumulation
951 rates and constrain changes in past ice-flow dynamics (c.f. Cavitte et al., 2018; Parrenin and
952 Hindmarsh, 2007; Siegert and Payne, 2004; Sutter et al., 2021).

953 We also expect this data release to be useful in a series of other ice-dynamical applications in
954 the future. Examples applied to individual BAS datasets so far include calculating balance velocities
955 from dated englacial layers (Rippin et al., 2003b), analyses of water routing systems and bed
956 reflectivity (Chu et al., 2021; Rippin et al., 2006), as well as assessments of the bed roughness and
957 local topography (Rippin et al., 2003a; 2011; 2014), amongst others. It is our aspiration that this data
958 release will enable further such studies in the future.

959 **5.2. Polar Airborne Geophysics Data Portal**

960 One specificity of the platform is that it offers three types of geophysical datasets - namely
961 gravity, magnetic and radar - at the same time geospatially. Although some surveys were acquired
962 over 25 years ago, they may never have been exploited or analysed fully in a form that reached peer-
963 reviewed publications, nor combined with other geophysical data before, increasing in turn their re-
964 usability. By publishing this resource, we anticipate that the portal and datasets will foster new
965 research and discoveries related to our understanding of ice-sheet processes and crust and lithosphere
966 heterogeneity beneath the Antarctic Ice Sheet.

967 Additionally, the portal enables users to combine the published line datasets with gridded
968 products to compare the ability of the interpolated datasets to match the direct observations. For
969 instance, as shown in Figure 10 for the 2012-13 ICEGRAV survey, the portal allows users to readily
970 investigate the free-air gravity anomaly with the bed topography from BEDMAP2 or assess the
971 consistency between the measured ICEGRAV magnetic anomalies and the gridded aeromagnetic
972 product (Fig. 10). Alternatively, the quick-look radargrams can be compared with the ice-thickness
973 and bed-elevation grid cells from BEDMAP to assess sub-km variations in along- and across-flow on
974 the radar data which may have been smoothed out in the 1-km gridded product.

975 With its ~207,000 line-km of gravity, ~338,000 line-km of magnetic, and ~352,000 line-km
976 of radar data published, the Polar Airborne Geophysics Data Portal provides a robust platform for the
977 dissemination of the BAS aerogeophysical data. Further opportunities offered by the data portal are
978 the potential for the platform to be used to plan future field surveys or encourage future compilation
979 efforts based on gaps in the data coverage or quality of the data.
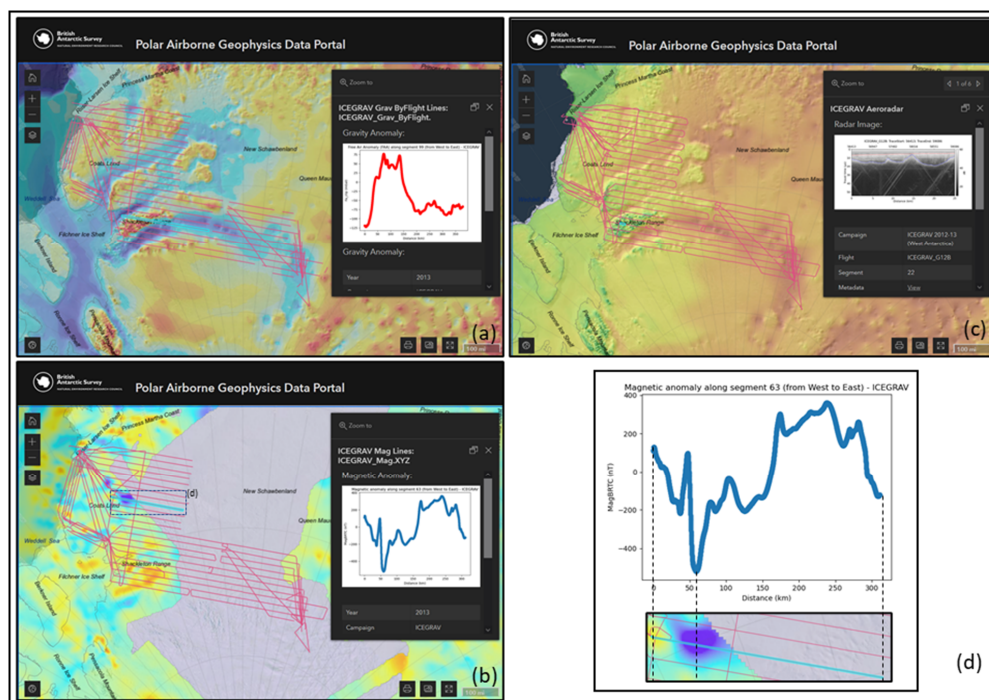
980
981 **Figure 10. Screenshots of the Polar Airborne Geophysics Data Portal showing the three**
982 **aerogeophysical products for the 2012-13 ICEGRAV survey with different basemaps.** (a) ICEGRAV
983 aerogravity survey with the BEDMAP2 bed elevation basemap (b) ICEGRAV aeromagnetic survey with the
984 magnetic anomaly basemap from Goodge and Finn (2010), (c) ICEGRAV aeroradar survey with the ice
985 thickness basemap from BEDMAP2. (d) Magnetic anomaly along the profile highlighted in (c) with a
986 comparison with the aeromagnetic anomaly map from Goodge and Finn (2010).

987

988 ### 5.3. Future Work

989 Although most of data published here have already been incorporated into previous data
990 compilations such as BEDMAP2 or ADMAP2, the more recent datasets presented here will provide
991 useful additions to future editions of such initiatives. Examples of this are the data acquired as part of
992 the 2012-13 ICEGRAV aeromagnetic campaign in Dronning Maud Land where the last compilation
993 effort of magnetic anomalies had shown a large gap (Goodge and Finn, 2010; Fig. 10), or the new ice-
994 thickness and bed-elevation data acquired over Thwaites Glacier (2018-20), South Pole (2015-16),
995 and Filchner Ice Shelf (2015-17) which are expected to be added to the new BEDMAP3 compilation.

996 Even though most of the gravity, magnetic and bed-pick data acquired since the mid-1990s
997 are now fully published, radar data from older surveys (1994-2004) for which the bed-pick data are
998 published and already integrated into larger gridded products (e.g. BEDMAP; Fretwell et al., 2013)
999 are yet to be published in full as per the more modern surveys (2004-2020) released here (see Table
1000 3). This is primarily due to poorer data management practices at times of acquisition and less well-
1001 documented processing procedures which restrict the re-usability of these older radar dataset. Much
1002 older analogue radar data acquired on films and video tapes prior to the deployment of digital radars
1003 (i.e. pre-1994) also offer additional opportunities, although the necessity for manual digitisation
1004 makes this task much more time consuming and challenging. It is worth noting, however, that many
1005 of the regions broadly covered by these older surveys have recently been re-flown using more modern

1006 instruments, much as part of NASA's Operation IceBridge programme (MacGregor et al., 2021),
1007 although reprocessing and modernising older radar data can bring substantial benefits, as already
1008 demonstrated by Schroeder et al. (2019). Additional reprocessing of older radar data using modern 2-
1009 D SAR techniques would also be beneficial, as recently demonstrated by Chu et al. (2021).

1010 Lastly, and as a result of the very flexible configuration of the PASIN-2 system, much more
1011 data can be extracted from the raw radar files already acquired, including fully polarised data used to
1012 image ice crystal-fabric orientation for estimating ice deformation processes (i.e. Young et al., 2021),
1013 or 3-D swath radar data used to reconstruct the sub-surface at finer resolution and without
1014 compromising on across-track resolution as for conventional 2-D data (Holschuh et al., 2020; Arenas-
1015 Pingarron et al., 2022).

1016 Combined, these will likely add further opportunities for future data releases, alongside our
1017 intention to publish newly acquired data regularly via the data portal and following the procedures
1018 detailed in this paper.

1019

1020 **6. Conclusion**

1021 We have presented here the release of 64 aerogeophysical datasets from 24 surveys flown by
1022 the British Antarctic Survey between 1994 and 2020 over the Antarctic Peninsula and East and West
1023 Antarctica. Altogether, the data release consists of ~450,000 line-km (or ~5.3.million km^2) of
1024 aerogeophysical data on gravity, magnetic and radar measurements (including bed-pick and the fully
1025 processed 2-D radar data) which have all been standardised according to the FAIR (Findable,
1026 Accessible, Interoperable and Re-Usable) data principles. A new data portal, the Polar Airborne
1027 Geophysics Data Portal (https://www.bas.ac.uk/project/nagdp/), and interactive, open-access tutorials
1028 written in Python and MATLAB have also been created to improve the interactivity and user-
1029 accessibility of our datasets.

1030 Aside from discussing the data acquisition and processing steps, we have demonstrated that
1031 much more information can be extracted from the full radar datasets by assessing the continuity of
1032 englacial layering along ~300,000 line-km of the newly released radar data. Using an automated layer
1033 continuity extraction method on all ten fully published 2-D radar datasets, we have shown that large
1034 volumes of radar profiles contain well-preserved englacial layering from which further information
1035 such as past accumulation rates and ice-dynamical processes can be extracted.

1036 Although all of the datasets released here have so far made a significant contribution to our
1037 understanding of past and current ice-dynamical and lithospheric influences, partly through their
1038 contributions to major international collaborative projects such as the SCAR BEDMAP and ADMAP
1039 programmes, they have until now largely remained unpublished in their full form thus restricting the
1040 further usage of the data beyond the life cycle of the science projects. It is our hope that these newly
1041 released data will offer further research opportunities and enable the wider geophysical and
1042 glaciological community to benefit from the abundance of newly published aerogeophysical data over
1043 Antarctica, particularly within the context of recently established international projects such as the
1044 SCAR AntArchitecture and RINGS Action groups.

1045 Reflecting on our collaboration between data managers and scientists, we believe that this
1046 project sets a positive example for further release of aerogeophysical data, particularly for future
1047 international initiatives that are aiming to harmonise the availability and findability of
1048 aerogeophysical data collected across Antarctica. A full list of all available datasets can be found in
1049 Table 3 of this paper, or via the BAS Discovery Metadata System (https://data.bas.ac.uk).

1050

Data Availability Statement

All the data included in this manuscript are freely available via the BAS Discovery Metadata System (https://data.bas.ac.uk), with direct links to the datasets found in Table 3 of this paper. The user guide for the data portal and the Jupiter Notebook tutorials designed for reading in the gravity, magnetic, and radar data in Python and MATLAB are freely accessible on the Jupiter Book interface (https://antarctica.github.io/PDC_GeophysicsBook) or via the BAS GitHub repository (https://github.com/antarctica/PDC_GeophysicsBook). The code used to produce the Internal Layer Continuity Index over the whole BAS radar dataset (Fig. 8-9) is available on the GitHub page of J.A.B. (https://github.com/julbod).

Competing Interests

The authors declare that they have no conflict of interest.

Contribution Statement

A.C.F. and J.A.B. co-led this data release. A.C.F. initiated the collaboration between the Polar Data Centre and the BAS Airborne Geophysics science team, with input from H.J.P. A.C.F. quality-checked and published the gravity, magnetic and bed-pick datasets, with input from T.A.J., F.F, and J.A.B. J.A.B re-processed, quality-checked, and published the fully processed radar datasets and accompanying files, with input from A.C.F., T.A.J. and C.R. The three BAS radar systems and accompanying radar processing software libraries were designed by H.F.J.C. The aerogeophysical data were primarily acquired and processed by H.F.J.C, C.R., F.F. and T.A.J. J.A.B created the data portal, with input from A.C.F., T.A.J. and F.F. A.C.F. and J.A.B. populated the data portal with the gravity, magnetic, and radar track-lines. A.C.F. created the Jupyter Notebook tutorials, with input from J.A.B. for the radar tutorials and user guide. J.A.B. wrote the code and analysed the results for the layer continuity index. J.A.B wrote the initial manuscript and created the figures, with input from A.C.F. All authors commented and contributed to the final edits of the manuscript prior to publication.

Acknowledgments

We would like to thank the many BAS personnel involved over the last three decades in developing and maintaining the aerogeophysical instruments and in acquiring and processing the data presented in this paper. In particular, we would like to credit and acknowledge Hugh Corr and Nick Frearson for designing the PASIN radar systems. We are also especially grateful to the many pilots that flew the BAS Twin Otter aicraft "VP-FBL" throughout the years, including Lee Proudfoot, Greg Harris, Pete Buckley, Doug Pearson, Mark Beasley, Doug Cochrane, Andy Vidamour, Oli Smith, and particularly David Leatherdale and Ian Potten who flew most of the survey km. Many campaigns that BAS conducted were also in partnership with international collaborators and institutes from around the world, which we would also like to acknowledge more widely. J.A.B was partly funded by the NERC Doctoral Training Partnership (grant reference number: NE/L002558/1) hosted in the Edinburgh E^3 DTP program. We would also like to acknowledge the help from the BAS PDC and MAGIC (Mapping and GIS) teams for their valuable input throughout this project.

References

1093   Arenas-Pingarron A., Corr H.J.W., Robinson C., Jordan T.A., and Brennan P.V., 2022.
1094 PASIN2, an Ice-Sounding Airborne Synthetic Aperture Radar for Subglacial 3D Imagery. *IET*
1095 *RADAR SONAR NAV.* (In review).

1096

1097   Arndt, J.E., Schenke, H.W., Jakobsson, M., Nitsche, F.O., Buys, G., Goleby, B., Rebesco, M.,
1098 Bohoyo, F., Hong, J., Black, J. and Greku, R., 2013. The International Bathymetric Chart of the
1099 Southern Ocean (IBCSO) Version 1.0—A new bathymetric compilation covering circum-Antarctic
1100 waters. *GEOPHYS RES LETT*, *40*(12), pp.3111-3117. https://doi.org/10.1002/grl.50413

1101

1102   Ashmore, D.W., Bingham, R.G., Hindmarsh, R.C., Corr, H.F. and Joughin, I.R., 2014. The
1103 relationship between sticky spots and radar reflectivity beneath an active West Antarctic ice stream.
1104 *ANN GLACIOL*, 55(67), pp.29-38. https://doi.org/10.3189/2014AoG67A052

1105

1106   Ashmore, D.W. and Bingham, R.G., 2014. Antarctic subglacial hydrology: current knowledge
1107 and future challenges. *ANTARCT SCI*, *26*(6), pp.758-773.
1108 https://doi.org/10.1017/S0954102014000546

1109

1110   Ashmore, D.W., Bingham, R.G., Ross, N., Siegert, M.J., Jordan, T.A. and Mair, D.W., 2020.
1111 Englacial architecture and age-depth constraints across the West Antarctic Ice Sheet. *GEOPHYS RES*
1112 *LETT*, 47(6), p.e2019GL086663. https://doi.org/10.1029/2019GL086663

1113

1114   Bamber, J.L., Ferraccioli, F., Joughin, I., Shepherd, T., Rippin, D.M., Siegert, M.J. and
1115 Vaughan, D.G., 2006. East Antarctic ice stream tributary underlain by major sedimentary basin.
1116 *GEOLOGY*, 34(1), pp.33-36. https://doi.org/10.1130/G22160.1

1117

1118   Becker, D., Nielsen, J.E., Ayres-Sampaio, D., Forsberg, R., Becker, M. and Bastos, L., 2015.
1119 Drift reduction in strapdown airborne gravimetry using a simple thermal correction. *J*
1120 *GEODESY*, *89*(11), pp.1133-1144. https://doi.org/10.1007/s00190-015-0839-8

1121

1122   Bell, R.E., Blankenship, D.D., Finn, C.A., Morse, D.L., Scambos, T.A., Brozena, J.M. and
1123 Hodge, S.M., 1998. Influence of subglacial geology on the onset of a West Antarctic ice stream from
1124 aerogeophysical observations. *NATURE*, *394*(6688), pp.58-62. https://doi.org/10.1038/27883

1125

1126   Bell, R.E., Studinger, M., Fahnestock, M.A. and Shuman, C.A., 2006. Tectonically controlled
1127 subglacial lakes on the flanks of the Gamburtsev Subglacial Mountains, East Antarctica. *GEOPHYS*
1128 *RES LETT*, *33*(2). https://doi.org/10.1029/2005GL025207

1129

1130   Bell, R.E., Ferraccioli, F., Creyts, T.T., Braaten, D., Corr, H., Das, I., Damaske, D., Frearson,
1131 N., Jordan, T., Rose, K. and Studinger, M., 2011. Widespread persistent thickening of the East

Antarctic Ice Sheet by freezing from the base. *SCIENCE*, 331(6024), pp.1592-1595.
https://doi.org/10.1126/science.1200109

Bindschadler, R., Vornberger, P., Fleming, A., Fox, A., Mullins, J., Binnie, D., Paulsen, S.J.,
Granneman, B. and Gorodetzky, D., 2008. The Landsat image mosaic of Antarctica. *REMOTE SENS
ENVIRON*, 112(12), pp.4214-4226. https://doi.org/10.1016/j.rse.2008.07.006

Bindschadler, R.A.; Choi, H., Wichlacz, A, Bingham, R., Bohlander, J., Brunt, K., Corr, H.,
Drews, R., Fricker, H., Hall, M., Hindmarsh, R., Kohler, J., Padman, L., Rack, W., Rotschky, G.,
Urbini, S., Vornberger, P. and Young, N. (2011) Getting around Antarctica: New high-resolution
mappings of the grounded and freely-floating boundaries of the Antarctic ice sheet created for the
International Polar Year. *THE CRYOSPHERE*, 5, 569-588. https://doi.org/10.5194/tc-5-569-2011

Bingham, R.G., Siegert, M.J., Young, D.A. and Blankenship, D.D., 2007. Organized flow
from the South Pole to the Filchner-Ronne ice shelf: An assessment of balance velocities in interior
East Antarctica using radio echo sounding data. *J GEOPHYS RES-EARTH*, *112*(F3).
https://doi.org/10.1029/2006JF000556

Bingham, R.G., Ferraccioli, F., King, E.C., Larter, R.D., Pritchard, H.D., Smith, A.M. and
Vaughan, D.G., 2012. Inland thinning of West Antarctic Ice Sheet steered along subglacial rifts.
NATURE, 487(7408), pp.468-471. https://doi.org/10.1038/nature11292

Bingham, R.G., Rippin, D.M., Karlsson, N.B., Corr, H.F., Ferraccioli, F., Jordan, T.A., Le
Brocq, A.M., Rose, K.C., Ross, N. and Siegert, M.J., 2015. Ice-flow structure and ice dynamic
changes in the Weddell Sea sector of West Antarctica from radar-imaged internal layering. *J
GEOPHYS RES-EARTH*, *120*(4), pp.655-670. https://doi.org/10.1002/2014JF003291

Blankenship, D.D., Morse, D.L., Finn, C.A., Bell, R.E., Peters, M.E., Kempf, S.D., Hodge,
S.M., Studinger, M., Behrendt, J.C. and Brozena, J.M., 2001. Geologic controls on the initiation of
rapid basal motion for West Antarctic ice streams: A geophysical perspective including new airborne
radar sounding and laser altimetry results. *THE WEST ANTARCTIC ICE SHEET: BEHAVIOR AND
ENVIRONMENT*, 77, pp.105-121. https://doi.org/10.1029/AR077p0105

Blankenship, D. D., S. D. Kempf, D. A. Young, T. G. Richter, D. M. Schroeder, J. S.
Greenbaum, T. van Ommen, R. C. Warner, J. L. Roberts, N. W. Young, E. Lemeur, M. J. Siegert, and
J. W. Holt. (2017) *IceBridge HiCARS 1 L1B Time-Tagged Echo Strength Profiles, Version 1.*
Boulder, Colorado USA. NASA National Snow and Ice Data Center Distributed Active Archive
Center. https://doi.org/10.5067/W2KXX0MYNJ9G

Bodart, J.A., Bingham, R.G., Ashmore, D.W., Karlsson, N.B., Hein, A.S. and Vaughan, D.G.,
2021. Age-depth stratigraphy of Pine Island Glacier inferred from airborne radar and ice-core

chronology. *J GEOPHYS RES-EARTH*, 126(4), p.e2020JF005927.
https://doi.org/10.1029/2020JF005927

Bozzo, E. and Ferraccioli, F., 2007. The Italian-British Antarctic geophysical and geological
survey in northern Victoria Land 2005-06-towards the International Polar Year 2007-08.
https://nora.nerc.ac.uk/id/eprint/15403

Buizert, C., Cuffey, K.M., Severinghaus, J.P., Baggenstos, D., Fudge, T.J., Steig, E.J.,
Markle, B.R., Winstrup, M., Rhodes, R.H., Brook, E.J. and Sowers, T.A., 2015. The WAIS Divide
deep ice core WD2014 chronology–Part 1: Methane synchronization (68–31 ka BP) and the gas age–
ice age difference. *CLIM PAST*, *11*(2), pp.153-173. https://doi.org/10.5194/cp-11-153-2015

Cavitte, M.G., Parrenin, F., Ritz, C., Young, D.A., Van Liefferinge, B., Blankenship, D.D.,
Frezzotti, M. and Roberts, J.L., 2018. Accumulation patterns around Dome C, East Antarctica, in the
last 73 kyr. *THE CRYOSPHERE*, *12*(4), pp.1401-1414. https://doi.org/10.5194/tc-12-1401-2018

Chu, W., Hilger, A.M., Culberg, R., Schroeder, D.M., Jordan, T.M., Seroussi, H., Young,
D.A., Blankenship, D.D. and Vaughan, D.G., 2021. Multi-system synthesis of radar sounding
observations of the Amundsen Sea sector from the 2004-2005 field season. *J GEOPHYS RES-
EARTH*, p.e2021JF006296. https://doi.org/10.1029/2021JF006296

Constantino, R.R., Tinto, K.J., Bell, R.E., Porter, D.F. and Jordan, T.A., 2020. Seafloor depth
of George VI Sound, Antarctic Peninsula, from inversion of aerogravity data. *GEOPHYS RES LETT*,
47(21), p.e2020GL088654. https://doi.org/10.1029/2020GL088654

Corr, H. and Popple, M., 1994. Airborne radio echo sounding on the Evans flowline, Ronne
Ice Shelf. *Filchner-Ronne Ice Shelf Programme Report*, *8*, pp.9-11.
http://nora.nerc.ac.uk/id/eprint/515954

Corr, H.F., Ferraccioli, F., Frearson, N., Jordan, T., Robinson, C., Armadillo, E., Caneva, G.,
Bozzo, E. and Tabacco, I., 2007. Airborne radio-echo sounding of the Wilkes Subglacial Basin, the
Transantarctic Mountains and the Dome C region. *TERRA ANT REPORTS*, 13, pp.55-63.
https://nora.nerc.ac.uk/id/eprint/13578

Corr, H.F. and Vaughan, D.G., 2008. A recent volcanic eruption beneath the West Antarctic
ice sheet. *NAT GEOSCI*, 1(2), pp.122-125. https://doi.org/10.1038/ngeo106

Creyts, T.T., Ferraccioli, F., Bell, R.E., Wolovick, M., Corr, H., Rose, K.C., Frearson, N.,
Damaske, D., Jordan, T., Braaten, D. and Finn, C., 2014. Freezing of ridges and water networks

1212 preserves the Gamburtsev Subglacial Mountains for millions of years. *GEOPHYS RES LETT,* 41(22),
1213 pp.8114-8122. https://doi.org/10.1002/2014GL061491

1214

1215 Delf, R., Schroeder, D.M., Curtis, A., Giannopoulos, A. and Bingham, R.G., 2020. A
1216 comparison of automated approaches to extracting englacial-layer geometry from radar data across ice
1217 sheets. *ANN GLACIOL*, *61*(81), pp.234-241. https://doi.org/10.1017/aog.2020.42

1218

1219 Diez, A., Matsuoka, K., Ferraccioli, F., Jordan, T.A., Corr, H.F., Kohler, J., Olesen, A.V. and
1220 Forsberg, R., 2018. Basal settings control fast ice flow in the Recovery/Slessor/Bailey Region, East
1221 Antarctica. *GEOPHYS RES LETT*, *45*(6), pp.2706-2715. https://doi.org/10.1002/2017GL076601

1222

1223 Diez, A., Matsuoka, K., Jordan, T.A., Kohler, J., Ferraccioli, F., Corr, H.F., Olesen, A.V.,
1224 Forsberg, R. and Casal, T.G., 2019. Patchy lakes and topographic origin for fast flow in the Recovery
1225 Glacier system, East Antarctica. *J GEOPHYS RES-EARTH*, *124*(2), pp.287-304.
1226 https://doi.org/10.1029/2018JF004799

1227

1228 EPICA Community Members, 2004. Eight glacial cycles from an Antarctic ice core.
1229 *NATURE*, *429*, pp.623-628. https://doi.org/10.1038/nature02599

1230

1231 Ferraccioli, F., Gambetta, M. & Bozzo, E., 1998. Microlevelling procedures applied to
1232 regional aeromagnetic data: an example from the Transantarctic Mountains (Antarctica), *GEOPHYS*
1233 *PROSPECT*, 46, 177-196, https://doi.org/10.1046/j.1365-2478.1998.00080.x

1234

1235 Ferraccioli, F., Jones, P.C., Curtis, M.L. and Leat, P.T., 2005a. Subglacial imprints of early
1236 Gondwana break-up as identified from high resolution aerogeophysical data over western Dronning
1237 Maud Land, East Antarctica. *TERRA NOVA*, *17*(6), pp.573-579. https://doi.org/10.1111/j.1365-
1238 3121.2005.00651.x

1239

1240 Ferraccioli, F., PC, J., ML, C., PT, L. and TR, R., 2005b. Tectonic and magmatic patterns in
1241 the Jutulstraumen rift (?) region, East Antarctica, as imaged by high-resolution aeromagnetic data.
1242 *EARTH, PLANETS AND SPACE*, *57*(8), pp.767-780. https://doi.org/10.1186/BF03351856

1243

1244 Ferraccioli, F., Jones, P.C., Vaughan, A.P.M. and Leat, P.T., 2006. New aerogeophysical
1245 view of the Antarctic Peninsula: More pieces, less puzzle. *GEOPHYS RES LETT*, *33*(5).
1246 https://doi.org/10.1029/2005GL024636

1247

1248 Ferraccioli, F., Jordan, T., Armadillo, E., Bozzo, E., Corr, H., Caneva, G., Robinson, C.,
1249 Frearson, N. and Tabacco, I., 2007. Collaborative aerogeophysical campaign targets the Wilkes
1250 Subglacial Basin, the Transantarctic Mountains and the Dome C region. *TERRA ANT REPORTS*, *13*,
1251 pp.1-36. https://nora.nerc.ac.uk/id/eprint/13741

1252

1253   Ferraccioli, F., Armadillo, E., Jordan, T., Bozzo, E. and Corr, H., 2009. Aeromagnetic
1254   exploration over the East Antarctic Ice Sheet: a new view of the Wilkes Subglacial Basin.
1255   *TECTONOPHYSICS*, *478*(1-2), pp.62-77. https://doi.org/10.1016/j.tecto.2009.03.013

1256

1257   Ferraccioli, F., Finn, C.A., Jordan, T.A., Bell, R.E., Anderson, L.M. and Damaske, D., 2011.
1258   East Antarctic rifting triggers uplift of the Gamburtsev Mountains. *NATURE*, 479(7373), pp.388-392.
1259   https://doi.org/10.1038/nature10566

1260

1261   Ferris, J.K., Vaughan, A.P. and King, E.C., 2002. A window on West Antarctic crustal
1262   boundaries: the junction between the Antarctic Peninsula, the Filchner Block, and Weddell Sea
1263   oceanic lithosphere. *TECTONOPHYSICS*, 347(1-3), pp.13-23. https://doi.org/10.1016/S0040-
1264   1951(01)00235-9

1265

1266   Ferris, J.K., Storey, B.C., Vaughan, A.P., Kyle, P.R. and Jones, P.C., 2003. The Dufek and
1267   Forrestal intrusions, Antarctica: A centre for Ferrar large igneous province dike emplacement?.
1268   *GEOPHYS RES LETT*, 30(6). https://doi.org/10.1029/2002GL016719

1269

1270   Forsberg, R., Olesen, A.V., Ferraccioli, F., Jordan, T.A., Matsuoka, K., Zakrajsek, A.,
1271   Ghidella, M. and Greenbaum, J.S., 2018. Exploring the Recovery Lakes region and interior Dronning
1272   Maud Land, East Antarctica, with airborne gravity, magnetic and radar measurements.
1273   *GEOLOGICAL SOCIETY, LONDON, SPECIAL PUBLICATIONS*, *461*(1), pp.23-34.
1274   https://doi.org/10.1144/SP461.17

1275

1276   Frederick, B.C., Young, D.A., Blankenship, D.D., Richter, T.G., Kempf, S.D., Ferraccioli, F.
1277   and Siegert, M.J., 2016. Distribution of subglacial sediments across the Wilkes Subglacial Basin, East
1278   Antarctica. *J GEOPHYS RES-EARTH*, 121(4), pp.790-813. https://doi.org/10.1002/2015JF003760

1279

1280   Fretwell, P., Pritchard, H.D., Vaughan, D.G., Bamber, J.L., Barrand, N.E., Bell, R., Bianchi,
1281   C., Bingham, R.G., Blankenship, D.D., Casassa, G. and Catania, G., 2013. Bedmap2: improved ice
1282   bed, surface and thickness datasets for Antarctica. *THE CRYOSPHERE*, 7(1), pp.375-393.
1283   https://doi.org/10.5194/tc-7-375-2013

1284

1285   Global Change Master Directory (GCMD), 2021. *GCMD Keywords, Version 12.2.* Greenbelt,
1286   MD: Earth Science Data and Information System, Earth Science Projects Division, Goddard Space
1287   Flight Center (GSFC) National Aeronautics and Space Administration (NASA).
1288   *https://forum.earthdata.nasa.gov/app.php/tag/GCMD+Keywords* [Accessed: 01/12/2021].

1289

1290   Golynsky, A.V., Ferraccioli, F., Hong, J.K., Golynsky, D.A., von Frese, R.R.B., Young, D.A.,
1291   Blankenship, D.D., Holt, J.W., Ivanov, S.V., Kiselev, A.V. and Masolov, V.N., 2018. New magnetic

1292   anomaly map of the Antarctic. *GEOPHYS RES LETT*, *45*(13), pp.6437-6449.
1293   https://doi.org/10.1029/2018GL078153

1294

1295   Goodge, J.W. and Finn, C.A., 2010. Glimpses of East Antarctica: Aeromagnetic and satellite
1296   magnetic view from the central Transantarctic Mountains of East Antarctica. *J GEOPHYS RES-SOL*
1297   *EA*, *115*(B9). https://doi.org/10.1029/2009JB006890

1298

1299   Greenbaum, J.S., Blankenship, D.D., Young, D.A., Richter, T.G., Roberts, J.L., Aitken,
1300   A.R.A., Legresy, B., Schroeder, D.M., Warner, R.C., Van Ommen, T.D. and Siegert, M.J., 2015.
1301   Ocean access to a cavity beneath Totten Glacier in East Antarctica. *NAT GEOSCI*, 8(4), pp.294-298.
1302   https://doi.org/10.1038/ngeo2388

1303

1304   Hackney, R.I. and Featherstone, W.E., 2003. Geodetic versus geophysical perspectives of the
1305   'gravity anomaly'. *GEOPHYS J INT*, 154(1), pp.35-43. https://doi.org/10.1046/j.1365-
1306   246X.2003.01941.x

1307

1308   Harlan, R.B., 1968. Eotvos corrections for airborne gravimetry. *J GEOPHYS RES*, *73*(14),
1309   pp.4675-4679. https://doi.org/10.1029/JB073i014p04675

1310

1311   Hélière, F., Lin, C.C., Corr, H. and Vaughan, D., 2007. Radio echo sounding of Pine Island
1312   Glacier, West Antarctica: Aperture synthesis processing and analysis of feasibility from space. *IEEE*
1313   *T GEOSCI REMOTE*, *45*(8), pp.2573-2582. https://doi.org/10.1109/TGRS.2007.897433

1314

1315   Hodgson, D.A., Jordan, T.A., Rydt, J.D., Fretwell, P.T., Seddon, S.A., Becker, D., Hogan,
1316   K.A., Smith, A.M. and Vaughan, D.G., 2019. Past and future dynamics of the Brunt Ice Shelf from
1317   seabed bathymetry and ice shelf geometry. *THE CRYOSPHERE*, *13*(2), pp.545-556.
1318   https://doi.org/10.5194/tc-13-545-2019

1319

1320   Hofstede, C., Beyer, S., Corr, H., Eisen, O., Hattermann, T., Helm, V., Neckel, N., Smith,
1321   E.C., Steinhage, D., Zeising, O. and Humbert, A., 2021. Evidence for a grounding line fan at the onset
1322   of a basal channel under the ice shelf of Support Force Glacier, Antarctica, revealed by reflection
1323   seismics. *THE CRYOSPHERE*, *15*(3), pp.1517-1535. https://doi.org/10.5194/tc-15-1517-2021

1324

1325   Hogan, K.A., Larter, R.D., Graham, A.G., Arthern, R., Kirkham, J.D., Totten Minzoni, R.,
1326   Jordan, T.A., Clark, R., Fitzgerald, V., Wåhlin, A.K. and Anderson, J.B., 2020. Revealing the former
1327   bed of Thwaites Glacier using sea-floor bathymetry: implications for warm-water routing and bed
1328   controls on ice flow and buttressing. *THE CRYOSPHERE*, *14*(9), pp.2883-2908.
1329   https://doi.org/10.5194/tc-14-2883-2020

1330

1331   Holland, P.R., Corr, H.F., Vaughan, D.G., Jenkins, A. and Skvarca, P., 2009. Marine ice in
1332 Larsen ice shelf. *GEOPHYS RES LETT*, *36*(11). https://doi.org/10.1029/2009GL038162

1333

1334   Holland, P.R., Corr, H.F., Pritchard, H.D., Vaughan, D.G., Arthern, R.J., Jenkins, A. and
1335 Tedesco, M., 2011. The air content of Larsen ice shelf. *GEOPHYS RES LETT*, *38*(10).
1336 https://doi.org/10.1029/2011GL047245

1337

1338   Holschuh, N., Christianson, K., Paden, J., Alley, R.B. and Anandakrishnan, S., 2020. Linking
1339 postglacial landscapes to glacier dynamics using swath radar at Thwaites Glacier, Antarctica.
1340 *GEOLOGY*, *48*(3), pp.268-272. https://doi.org/10.1130/G46772.1

1341

1342   Holt, J.W., Blankenship, D.D., Morse, D.L., Young, D.A., Peters, M.E., Kempf, S.D.,
1343 Richter, T.G., Vaughan, D.G. and Corr, H.F., 2006. New boundary conditions for the West Antarctic
1344 Ice Sheet: Subglacial topography of the Thwaites and Smith glacier catchments. *GEOPHYS RES*
1345 *LETT*, *33*(9). https://doi.org/10.1029/2005GL025561

1346

1347   Howat, I.M., Porter, C., Smith, B.E., Noh, M.J. and Morin, P., 2019. The reference elevation
1348 model of Antarctica. *THE CRYOSPHERE*, *13*(2), pp.665-674. https://doi.org/10.5194/tc-13-665-2019

1349

1350   IPCC, 2021: Climate Change 2021: The Physical Science Basis. Contribution of Working
1351 Group I to the Sixth Assessment Report of the Intergovernmental Panel on Climate Change [Masson-
1352 Delmotte, V., P. Zhai, A. Pirani, S.L. Connors, C. Péan, S. Berger, N. Caud, Y. Chen, L. Goldfarb,
1353 M.I. Gomis, M. Huang, K. Leitzell, E. Lonnoy, J.B.R. Matthews, T.K. Maycock, T. Waterfield, O.
1354 Yelekçi, R. Yu, and B. Zhou (eds.)]. Cambridge University Press. In Press.

1355

1356   Jeofry, H., Ross, N., Corr, H.F., Li, J., Morlighem, M., Gogineni, P. and Siegert, M.J., 2018.
1357 A new bed elevation model for the Weddell Sea sector of the West Antarctic Ice Sheet. *EARTH SYST*
1358 *SCI DATA*, 10(2), pp.711-725. https://doi.org/10.5194/essd-10-711-2018

1359

1360   Johnson, A., Cheeseman, S. and Ferris, J., 1999. Improved compilation of Antarctic Peninsula
1361 magnetic data by new interactive grid suturing and blending methods. *ANN GEOPHYS-ITALY*, 42(2).
1362 https://doi.org/10.4401/ag-3717

1363

1364   Jones, P.C., Johnson, A.C., von Frese, R.R. and Corr, H., 2002. Detecting rift basins in the
1365 Evans Ice Stream region of West Antarctica using airborne gravity data. *TECTONOPHYSICS*, 347(1-
1366 3), pp.25-41. https://doi.org/10.1016/S0040-1951(01)00236-0

1367

1368   Jordan, T., Ferraccioli, F., Corr, H., Robinson, C., Caneva, G., Armadillo, E., Bozzo, E. and
1369 Frearson, N., 2007. Linking the Wilkes Subglacial Basin the Transantarctic Mountains and the Ross

Sea with a new airborne gravity survey. *TERRA ANT REPORTS*, *13*, pp.37-54.
https://nora.nerc.ac.uk/id/eprint/15749

Jordan, T.A., Ferraccioli, F., Jones, P.C., Smellie, J.L., Ghidella, M. and Corr, H., 2009.
Airborne gravity reveals interior of Antarctic volcano. *PHYS EARTH PLANET IN*, 175(3-4), pp.127-
136. https://doi.org/10.1016/j.pepi.2009.03.004

Jordan, T. A., Ferraccioli, F., Vaughan, D. G., Holt, J. W., Corr, H., Blankenship, D. D., &
Diehl, T. M. (2010). Aerogravity evidence for major crustal thinning under the Pine Island Glacier
region (West Antarctica). *BULLETIN*, *122*(5-6), 714-726. https://doi.org/10.1130/B26417.1

Jordan, T.A., Ferraccioli, F., Armadillo, E. and Bozzo, E., 2013. Crustal architecture of the
Wilkes Subglacial Basin in East Antarctica, as revealed from airborne gravity data.
TECTONOPHYSICS, 585, pp.196-206. https://doi.org/10.1016/j.tecto.2012.06.041

Jordan, T.A., Neale, R.F., Leat, P.T., Vaughan, A.P.M., Flowerdew, M.J., Riley, T.R.,
Whitehouse, M.J. and Ferraccioli, F., 2014. Structure and evolution of Cenozoic arc magmatism on
the Antarctic Peninsula: a high resolution aeromagnetic perspective. *GEOPHYS J INT*, *198*(3),
pp.1758-1774. https://doi.org/10.1093/gji/ggu233

Jordan, T.A., Martin, C., Ferraccioli, F., Matsuoka, K., Corr, H., Forsberg, R., Olesen, A. and
Siegert, M., 2018. Anomalously high geothermal flux near the South Pole. *SCI REP-UK*, *8*(1), pp.1-8.
https://doi.org/10.1038/s41598-018-35182-0

Jordan, T.A. and Becker, D., 2018. Investigating the distribution of magmatism at the onset of
Gondwana breakup with novel strapdown gravity and aeromagnetic data. *PHYS EARTH PLANET IN*,
282, pp.77-88. https://doi.org/10.1016/j.pepi.2018.07.007

Jordan, T.A., Porter, D., Tinto, K., Millan, R., Muto, A., Hogan, K., Larter, R.D., Graham,
A.G. and Paden, J.D., 2020. New gravity-derived bathymetry for the Thwaites, Crosson, and Dotson
ice shelves revealing two ice shelf populations. *THE CRYOSPHERE*, *14*(9), pp.2869-2882.
https://doi.org/10.5194/tc-14-2869-2020

Karlsson, N.B., Rippin, D.M., Vaughan, D.G. and Corr, H.F., 2009. The internal layering of
Pine Island Glacier, West Antarctica, from airborne radar-sounding data. *ANN GLACIOL*, 50(51),
pp.141-146. https://doi.org/3189/S0260305500250660

Karlsson, N.B., Rippin, D.M., Bingham, R.G. and Vaughan, D.G., 2012. A 'continuity-index'
for assessing ice-sheet dynamics from radar-sounded internal layers. *EARTH PLANET SC LETT*, 335,
pp.88-94. https://doi.org/10.1016/j.epsl.2012.04.034

1410

1411   Karlsson, N.B., Bingham, R.G., Rippin, D.M., Hindmarsh, R.C., Corr, H.F. and Vaughan,
1412   D.G., 2014. Constraining past accumulation in the central Pine Island Glacier basin, West Antarctica,
1413   using radio-echo sounding. *J GLACIOL*, 60(221), pp.553-562.
1414   https://doi.org/10.3189/2014JoG13j180

1415

1416   Karlsson, N.B., Binder, T., Eagles, G., Helm, V., Pattyn, F., Liefferinge, B.V. and Eisen, O.,
1417   2018. Glaciological characteristics in the Dome Fuji region and new assessment for "Oldest Ice".
1418   *THE CRYOSPHERE*, *12*(7), pp.2413-2424. https://doi.org/10.5194/tc-12-2413-2018

1419

1420   Lei, Y., Gardner, A.S. and Agram, P., 2021. Processing methodology for the ITS_LIVE
1421   Sentinel-1 ice velocity product. *EARTH SYST SCI DATA DISCUSSIONS*, pp.1-27.
1422   https://doi.org/10.5194/essd-2021-393

1423

1424   Le Brocq, A.M., Payne, A.J. and Vieli, A., 2010. An improved Antarctic dataset for high
1425   resolution numerical ice sheet models (ALBMAP v1). *EARTH SYST SCI DATA*, 2(2), pp.247-260.
1426   https://doi.org/10.5194/essd-2-247-2010

1427

1428   Luo, K., Liu, S., Guo, J., Wang, T., Li, L., Cui, X., Sun, B. and Tang, X., 2020. Radar-
1429   Derived Internal Structure and Basal Roughness Characterization along a Traverse from Zhongshan
1430   Station to Dome A, East Antarctica. *REMOTE SENSING*, 12(7), p.1079.
1431   https://doi.org/10.3390/rs12071079

1432

1433   Lythe, M.B. and Vaughan, D.G., 2001. BEDMAP: A new ice thickness and subglacial
1434   topographic model of Antarctica. *J GEOPHYS RES-SOL EA*, *106*(B6), pp.11335-11351.
1435   https://doi.org/10.1029/2000JB900449

1436

1437   MacGregor, J.A., Boisvert, L.N., Medley, B., Petty, A.A., Harbeck, J.P., Bell, R.E., Blair,
1438   J.B., Blanchard-Wrigglesworth, E., Buckley, E.M., Christoffersen, M.S. and Cochran, J.R., 2021. The
1439   scientific legacy of NASA's Operation Icebridge. *REV GEOPHYS*, *59*(2).
1440   https://doi.org/10.1029/2020RG000712

1441

1442   Millan, R., Rignot, E., Bernier, V., Morlighem, M. and Dutrieux, P., 2017. Bathymetry of the
1443   Amundsen Sea Embayment sector of West Antarctica from Operation IceBridge gravity and other
1444   data. *GEOPHYS RES LETT*, *44*(3), pp.1360-1368. https://doi.org/10.1002/2016GL072071

1445

1446   Moritz, H., 1980. Geodetic reference system 1980. *B GEOD*, *54*(3), pp.395-405.
1447   https://doi.org/10.1007/s001900050278

1448

Morlighem, M., C. Williams, E. Rignot, L. An, J. E. Arndt, J. Bamber, G. Catania, N. Chauché, J. A. Dowdeswell, B. Dorschel, I. Fenty, K. Hogan, I. Howat, A. Hubbard, M. Jakobsson, T. M. Jordan, K. K. Kjeldsen, R. Millan, L. Mayer, J. Mouginot, B. Noël, C. O'Cofaigh, S. J. Palmer, S. Rysgaard, H. Seroussi, M. J. Siegert, P. Slabon, F. Straneo, M. R. van den Broeke, W. Weinrebe, M. Wood, and K. Zinglersen. 2017. BedMachine v3: Complete bed topography and ocean bathymetry mapping of Greenland from multi-beam echo sounding combined with mass conservation. *GEOPHYS RES LETT*, 44. https://doi.org/10.1002/2017GL074954

Morlighem, M., Rignot, E., Binder, T., Blankenship, D., Drews, R., Eagles, G., Eisen, O., Ferraccioli, F., Forsberg, R., Fretwell, P. and Goel, V., 2020. Deep glacial troughs and stabilizing ridges unveiled beneath the margins of the Antarctic ice sheet. *NAT GEOSCI*, 13(2), pp.132-137. https://doi.org/10.1038/s41561-019-0510-8

Napoleoni, F., Jamieson, S.S., Ross, N., Bentley, M.J., Rivera, A., Smith, A.M., Siegert, M.J., Paxman, G.J., Gacitúa, G., Uribe, J.A. and Zamora, R., 2020. Subglacial lakes and hydrology across the Ellsworth Subglacial Highlands, West Antarctica. *THE CRYOSPHERE*, 14(12), pp.4507-4524. https://doi.org/10.5194/tc-14-4507-2020

Paden, J., J. Li, C. Leuschen, F. Rodriguez-Morales, and R. Hale. 2014, updated 2021. *IceBridge MCoRDS L1B Geolocated Radar Echo Strength Profiles, Version 2*. Boulder, Colorado USA. NASA National Snow and Ice Data Center Distributed Active Archive Center. https://doi.org/10.5067/90S1XZRBAX5N [Accessed: 01/12/2021].

Parrenin, F., Hindmarsh, R., 2007. Influence of a non-uniform velocity field on isochrone geometry along a steady flowline of an ice sheet. *J GLACIOL*, 53(183), 612-622. https://doi.org/10.3189/002214307784409298.

Paxman, G.J., Jamieson, S.S., Ferraccioli, F., Jordan, T.A., Bentley, M.J., Ross, N., Forsberg, R., Matsuoka, K., Steinhage, D., Eagles, G. and Casal, T.G., 2019. Subglacial Geology and Geomorphology of the Pensacola-Pole Basin, East Antarctica. *GEOCHEMISTRY, GEOPHYSICS, GEOSYSTEMS*, 20(6), pp.2786-2807. https://doi.org/10.1029/2018GC008126

Peters, M.E., Blankenship, D.D. and Morse, D.L., 2005. Analysis techniques for coherent airborne radar sounding: Application to West Antarctic ice streams. *J GEOPHYS RES-SOL EA, 110*(B6). https://doi.org/10.1029/2004JB003222

Rignot, E., Mouginot, J., & Scheuchl, B. (2017). *MEaSUREs InSAR-based Antarctica ice velocity map, version 2*. NASA National Snow and Ice Data Center Distributed Active Archive Center. https://doi.org/10.5067/D7GK8F5J8M8R

1489   Rippin, D.M., Bamber, J.L., Siegert, M.J., Vaughan, D.G. and Corr, H.F.J., 2003a. Basal
1490   topography and ice flow in the Bailey/Slessor region of East Antarctica. *J GEOPHYS RES-EARTH*,
1491   108(F1). https://doi.org/10.1029/2003JF000039

1492

1493   Rippin, D.M., Siegert, M.J. and Bamber, J.L., 2003b. The englacial stratigraphy of Wilkes
1494   Land, East Antarctica, as revealed by internal radio-echo sounding layering, and its relationship with
1495   balance velocities. *ANN GLACIOL*, *36*, pp.189-196. https://doi.org/10.3189/172756403781816356

1496

1497   Rippin, D.M., Bamber, J.L., Siegert, M.J., Vaughan, D.G. and Corr, H.F.J., 2006. Basal
1498   conditions beneath enhanced-flow tributaries of Slessor Glacier, East Antarctica. *J GLACIOL*,
1499   *52*(179), pp.481-490. https://doi.org/10.3189/172756506781828467

1500

1501   Rippin, D.M., Vaughan, D.G. and Corr, H.F., 2011. The basal roughness of Pine Island
1502   Glacier, West Antarctica. *J GLACIOL*, *57*(201), pp.67-76.
1503   https://doi.org/10.3189/002214311795306574

1504

1505   Rippin, D.M., Bingham, R.G., Jordan, T.A., Wright, A.P., Ross, N., Corr, H.F., Ferraccioli,
1506   F., Le Brocq, A.M., Rose, K.C. and Siegert, M.J., 2014. Basal roughness of the Institute and Möller
1507   Ice Streams, West Antarctica: Process determination and landscape interpretation.
1508   *GEOMORPHOLOGY*, *214*, pp.139-147. https://doi.org/10.1016/j.geomorph.2014.01.021

1509

1510   Robin, G.D.Q., Swithinbank, C.W.M. and Smith, B.M.E., 1970. Radio echo exploration of
1511   the Antarctic ice sheet. *INTERNATIONAL ASSOCIATION OF SCIENTIFIC HYDROLOGY*
1512   *PUBLICATION*, *86*, pp.97-115.

1513

1514   Robin, G.D.Q., Drewry, D.J. and Meldrum, D.T., 1977. International studies of ice sheet and
1515   bedrock. *PHILOS T ROY SOC B*, *279*(963), pp.185-196. https://doi.org/10.1098/rstb.1977.0081

1516

1517   Rose, K.C., Ferraccioli, F., Jamieson, S.S., Bell, R.E., Corr, H., Creyts, T.T., Braaten, D.,
1518   Jordan, T.A., Fretwell, P.T. and Damaske, D., 2013. Early east Antarctic Ice Sheet growth recorded in
1519   the landscape of the Gamburtsev Subglacial Mountains. *EARTH PLANET SC LETT*, 375, pp.1-12.
1520   https://doi.org/10.1016/j.epsl.2013.03.053

1521

1522   Rose, K.C., Ross, N., Bingham, R.G., Corr, H.F., Ferraccioli, F., Jordan, T.A., Le Brocq,
1523   A.M., Rippin, D.M. and Siegert, M.J., 2014. A temperate former West Antarctic ice sheet suggested
1524   by an extensive zone of subglacial meltwater channels. *GEOLOGY*, *42*(11), pp.971-974.
1525   https://doi.org/10.1130/G35980.1

1526

1527   Ross, N., Bingham, R.G., Corr, H.F., Ferraccioli, F., Jordan, T.A., Le Brocq, A., Rippin,
1528   D.M., Young, D., Blankenship, D.D. and Siegert, M.J., 2012. Steep reverse bed slope at the grounding

1529   line of the Weddell Sea sector in West Antarctica. *NAT GEOSCI*, 5(6), pp.393-396.
1530   https://doi.org/10.1038/ngeo1468

1531

1532   Ross, N., Jordan, T.A., Bingham, R.G., Corr, H.F., Ferraccioli, F., Le Brocq, A., Rippin,
1533   D.M., Wright, A.P. and Siegert, M.J., 2014. The Ellsworth subglacial highlands: inception and retreat
1534   of the West Antarctic Ice Sheet. *BULLETIN*, 126(1-2), pp.3-15. https://doi.org/10.1130/B30794.1

1535

1536   Scheinert, M., Ferraccioli, F., Schwabe, J., Bell, R., Studinger, M., Damaske, D., ... &
1537   Richter, T. D. (2016). New Antarctic gravity anomaly grid for enhanced geodetic and geophysical
1538   studies in Antarctica. *GEOPHYS RES LETT*, 43(2), 600-610. https://doi.org/10.1002/2015GL067439

1539

1540   Schroeder, D.M., Blankenship, D.D. and Young, D.A., 2013. Evidence for a water system
1541   transition beneath Thwaites Glacier, West Antarctica. *P NATL A SCI*, 110(30), pp.12225-12228.
1542   https://doi.org/10.1073/pnas.1302828110

1543

1544   Schroeder, D.M., Blankenship, D.D., Young, D.A. and Quartini, E., 2014. Evidence for
1545   elevated and spatially variable geothermal flux beneath the West Antarctic Ice Sheet. *P NATL A SCI*,
1546   111(25), pp.9070-9072. https://doi.org/10.1073/pnas.1405184111

1547

1548   Schroeder, D.M., Dowdeswell, J.A., Siegert, M.J., Bingham, R.G., Chu, W., MacKie, E.J.,
1549   Siegfried, M.R., Vega, K.I., Emmons, J.R. and Winstein, K., 2019. Multidecadal observations of the
1550   Antarctic ice sheet from restored analog radar records. *P NATL A SCI*, 116(38), pp.18867-18873.
1551   https://doi.org/10.1073/pnas.1821646116

1552

1553   Shepherd, T., Bamber, J.L. and Ferraccioli, F., 2006. Subglacial geology in Coats Land, East
1554   Antarctica, revealed by airborne magnetics and radar sounding. *EARTH PLANET SC LETT*, 244(1-2),
1555   pp.323-335. https://doi.org/10.1016/j.epsl.2006.01.068

1556

1557   Siegert, M.J., Payne, A.J. and Joughin, I., 2003. Spatial stability of Ice Stream D and its
1558   tributaries, West Antarctica, revealed by radio-echo sounding and interferometry. *ANN GLACIOL*, 37,
1559   pp.377-382. https://doi.org/10.3189/172756403781816022

1560

1561   Siegert, M.J. and Payne, A.J., 2004. Past rates of accumulation in central West Antarctica.
1562   *GEOPHYS RES LETT*, 31(12). https://doi.org/10.1029/2004GL020290

1563

1564   Siegert, M., Ross, N., Corr, H., Kingslake, J. and Hindmarsh, R., 2013. Late Holocene ice-
1565   flow reconfiguration in the Weddell Sea sector of West Antarctica. *QUATERNARY SCI REV*, 78,
1566   pp.98-107. https://doi.org/10.1016/j.quascirev.2013.08.003

1567

1568   Siegert, M.J., Ross, N., Corr, H., Smith, B., Jordan, T., Bingham, R.G., Ferraccioli, F.,
1569 Rippin, D.M. and Le Brocq, A., 2014. Boundary conditions of an active West Antarctic subglacial
1570 lake: implications for storage of water beneath the ice sheet. *THE CRYOSPHERE*, *8*(1), pp.15-24.
1571 https://doi.org/10.5194/tc-8-15-2014

1572

1573   Sigl, M., Fudge, T.J., Winstrup, M., Cole-Dai, J., Ferris, D., McConnell, J.R., Taylor, K.C.,
1574 Welten, K.C., Woodruff, T.E., Adolphi, F. and Bisiaux, M., 2016. The WAIS Divide deep ice core
1575 WD2014 chronology–Part 2: Annual-layer counting (0–31 ka BP). *CLIM PAST*, *12*(3), pp.769-786.
1576 https://doi.org/10.5194/cp-12-769-2016

1577

1578   Sime, L.C., Karlsson, N.B., Paden, J.D. and Prasad Gogineni, S., 2014. Isochronous
1579 information in a Greenland ice sheet radio echo sounding data set. *GEOPHYS RES LETT*, *41*(5),
1580 pp.1593-1599. https://doi.org/10.1002/2013GL057928

1581

1582   Studinger, M., Bell, R.E., Blankenship, D.D., Finn, C.A., Arko, R.A., Morse, D.L. and
1583 Joughin, I., 2001. Subglacial sediments: A regional geological template for ice flow in West
1584 Antarctica. *GEOPHYS RES LETT*, *28*(18), pp.3493-3496. https://doi.org/10.1029/2000GL011788

1585

1586   Sutter, J., Fischer, H. and Eisen, O., 2021. Investigating the internal structure of the Antarctic
1587 ice sheet: the utility of isochrones for spatiotemporal ice-sheet model calibration. *THE
1588 CRYOSPHERE*, 15, 3839-3860. https://doi.org/10.5194/tc-15-3839-2021

1589

1590   Tinto, K.J. and Bell, R.E., 2011. Progressive unpinning of Thwaites Glacier from newly identified
1591 offshore ridge: Constraints from aerogravity. *GEOPHYS RES LETT*, 38(20).
1592 https://doi.org/10.1029/2011GL049026

1593

1594   Tinto, K.J., Padman, L., Siddoway, C.S., Springer, S.R., Fricker, H.A., Das, I., Tontini, F.C.,
1595 Porter, D.F., Frearson, N.P., Howard, S.L. and Siegfried, M.R., 2019. Ross Ice Shelf response to
1596 climate driven by the tectonic imprint on seafloor bathymetry. *NAT GEOSCI*, *12*(6), pp.441-449.
1597 https://doi.org/10.1038/s41561-019-0370-2

1598

1599   Valliant, H.D., 1992. LaCoste & Romberg Air/Sea Meters: An Overview, CRC Handbook of
1600 Geophysical Exploration at Sea. London, CRC Press.

1601

1602   Vaughan, D.G., Corr, H.F., Ferraccioli, F., Frearson, N., O'Hare, A., Mach, D., Holt, J.W.,
1603 Blankenship, D.D., Morse, D.L. and Young, D.A., 2006. New boundary conditions for the West
1604 Antarctic ice sheet: Subglacial topography beneath Pine Island Glacier. *GEOPHYS RES LETT*, 33(9).
1605 https://doi.org/10.1029/2005GL025588

1606

1607   Vaughan, D.G., Corr, H.F., Bindschadler, R.A., Dutrieux, P., Gudmundsson, G.H., Jenkins,
1608 A., Newman, T., Vornberger, P. and Wingham, D.J., 2012. Subglacial melt channels and fracture in
1609 the floating part of Pine Island Glacier, Antarctica. *J GEOPHYS RES-EARTH*, *117*(F3).
1610 https://doi.org/10.1029/2012JF002360

1611

1612   Wilkinson, M.D., Dumontier, M., Aalbersberg, I.J., Appleton, G., Axton, M., Baak, A.,
1613 Blomberg, N., Boiten, J.W., da Silva Santos, L.B., Bourne, P.E. and Bouwman, J., 2016. The FAIR
1614 Guiding Principles for scientific data management and stewardship. *SCI. DATA*, *3*(1), pp.1-9.
1615 https://doi.org/10.1038/sdata.2016.18

1616
1617   Winter, K., Woodward, J., Ross, N., Dunning, S.A., Bingham, R.G., Corr, H.F. and Siegert,
1618 M.J., 2015. Airborne radar evidence for tributary flow switching in Institute Ice Stream, West
1619 Antarctica: Implications for ice sheet configuration and dynamics. *J GEOPHYS RES-EARTH*, *120*(9),
1620 pp.1611-1625. https://doi.org/10.1002/2015JF003518
1621
1622   Winter, K., Ross, N., Ferraccioli, F., Jordan, T.A., Corr, H.F., Forsberg, R., Matsuoka, K.,
1623 Olesen, A.V. and Casal, T.G., 2018. Topographic steering of enhanced ice flow at the bottleneck
1624 between East and West Antarctica. *GEOPHYS RES LETT*, *45*(10), pp.4899-4907.
1625 https://doi.org/10.1029/2018GL077504
1626
1627   Wright, A.P., Young, D.A., Roberts, J.L., Schroeder, D.M., Bamber, J.L., Dowdeswell, J.A.,
1628 Young, N.W., Le Brocq, A.M., Warner, R.C., Payne, A.J. and Blankenship, D.D., 2012. Evidence of a
1629 hydrological connection between the ice divide and ice sheet margin in the Aurora Subglacial Basin,
1630 East Antarctica. *J GEOPHYS RES-EARTH*, *117*(F1). https://doi.org/10.1029/2011JF002066
1631
1632   Young, D.A., Schroeder, D.M., Blankenship, D.D., Kempf, S.D. and Quartini, E., 2016. The
1633 distribution of basal water between Antarctic subglacial lakes from radar sounding. *Philosophical
1634 Transactions of the Royal Society A: Mathematical, Physical and Engineering Sciences*, *374*(2059),
1635 p.20140297. https://doi.org/10.1098/rsta.2014.0297
1636
1637   Young, T.J., Schroeder, D.M., Jordan, T.M., Christoffersen, P., Tulaczyk, S.M., Culberg, R.
1638 and Bienert, N.L., 2021. Inferring ice fabric from birefringence loss in airborne radargrams:
1639 Application to the eastern shear margin of Thwaites Glacier, West Antarctica. *J GEOPHYS RES-
1640 EARTH*, *126*(5), p.e2020JF006023. https://doi.org/10.1029/2020JF006023
1641